# Near-Infrared Fluorescent Micelles from Poly(norbornene) Brush Triblock Copolymers for Nanotheranostics

Carolyne B. Braga, † Ronaldo A. Pilli, † Catia Ornelas, † and Marcus Weck †

†Institute of Chemistry, University of Campinas (UNICAMP), P.O. Box 6154, CEP 13083-970, Campinas, SP, Brazil ‡Molecular Design Institute and Department of Chemistry, New York University, 100 Washington Square East, New York, NY 10003, United States

KEYWORDS: ROMP, brush block copolymers, piplartine, polymeric micelles, cyanine dye, anticancer, nanotheranostics

ABSTRACT: This contribution describes the design and synthesis of multifunctional micelles based on amphiphilic brush block copolymers (BBCPs) for imaging and selective drug delivery of natural anticancer compounds. Well-defined BBCPs were synthesized via one-pot multistep sequential graft-through ring-opening metathesis polymerization (ROMP) of norbornene-based macroinitiators. The norbornenes employed contain a poly(ethylene glycol) (PEG) methyl ether chain, an alkyl bromide chain, and/or a near-infrared (NIR) fluorescent cyanine dye. After block copolymerization, post-polymerization transformations using bromide-azide substitution followed by the strained-promoted alkyne-azide cycloaddition (SPAAC) allowed for the functionalization of the BBCPs with piplartine (PPT) moiety, a natural product with welldocumented cytotoxicity against cancer cell lines, via an ester linker between the drug and the polymer side-chain. The amphiphilic BBCPs selfassembled in aqueous media into nano-sized spherical micelles with neutral surface charges, as confirmed by dynamic light scattering (DLS) analysis and transmission electron microscopy (TEM). During self-assembly, paclitaxel (PTX) could be effectively encapsulated into the hydrophobic core to form stable PTX-loaded micelles with high loading capacities and encapsulation efficiencies. The NIR fluorescent dye containing micelles exhibited remarkable photophysical properties, excellent colloidal stability in physiological conditions, and a pH-induced disassembly at slightly acidic conditions, allowing for the release of the drug in a controlled manner. The in vitro studies demonstrated that the micelles without drug (blank micelles) are biocompatible at concentrations of up to 1 mg mL<sup>-1</sup> and present high cellular internalization capacity towards MCF-7 cancer cells. The drug-functionalized micelles showed in vitro cytotoxicity comparable to free PPT and PTX against MCF-7 and PC3 cancer cells, confirming efficient drug release in the tumor environment upon cellular internalization. Furthermore, the drug-functionalized micelles exhibited higher selectivity than the pristine drugs and preferential cellular uptake in human cancer cell lines (MCF-7 and PC3) when compared to normal breast cell line (MCF10A). This study provides an efficient strategy for the development of versatile polymeric nanosystems for drug delivery and image-guided diagnostic. Notably, the easy functionalization of BBCPs side-chains via SPAAC opens the possibility for the preparation of a library of multifunctional systems containing other drugs or functionalities, such as target groups for recognition.

# INTRODUCTION

Chemotherapy is currently the most widely adopted strategy for treating various types of cancer, playing a fundamental role both in cure and in extension of patients' survival. 1,2 Owing to the lack of targeting capability and nonspecific accumulation, however, chemotherapeutic agents are non-specific and attack non-cancer cells, leading to acute side-effects. In addition, since most anticancer compounds have low water solubility and consequently limited bioavailability, they require to be solubilized using high concentrations of surfactants or co-solvents, frequently leading to adverse effects. 3,4 These limitations compromise the success of treatments and recent research efforts have focused on developing new and more precise delivery strategies.

Research in cancer nanomedicine has achieved significant progress in recent years through the development of nanocarriers that improve biodistribution, effectiveness, tumor targeting and accumulation thereby enabling to enhance the balance between therapeutic

efficacy, selectivity, and overall toxicity of chemotherapeutic drugs.<sup>5-</sup> <sup>9</sup> Since the successful development of Doxil® (PEGylated liposomes containing doxorubicin) as the first FDA-approved nano-drug, 10 a range of nanomedicines have received regulatory approval or are under clinical investigation for the treatment of various types of cancer. 11-13 Nanomaterial-based drug delivery systems have shown prominent accumulation in tumors mediated by the enhanced permeability and retention (EPR) effect, which is based on the high permeability of the tumor vasculature to nanomedicines due to disordered endothelial cells and large fenestrations, in addition to the poorly lymphatic drainage in tumor tissues that causes the retention of the nanomaterials. 5,7,9 To exploit the EPR-based tumor targeting following systemic delivery, physicochemical properties of nanocarriers such as size, surface charge, and shape have to be controlled to allow for selective extravasation into tumors based on anatomical differences between normal and diseased tissues, to avoid

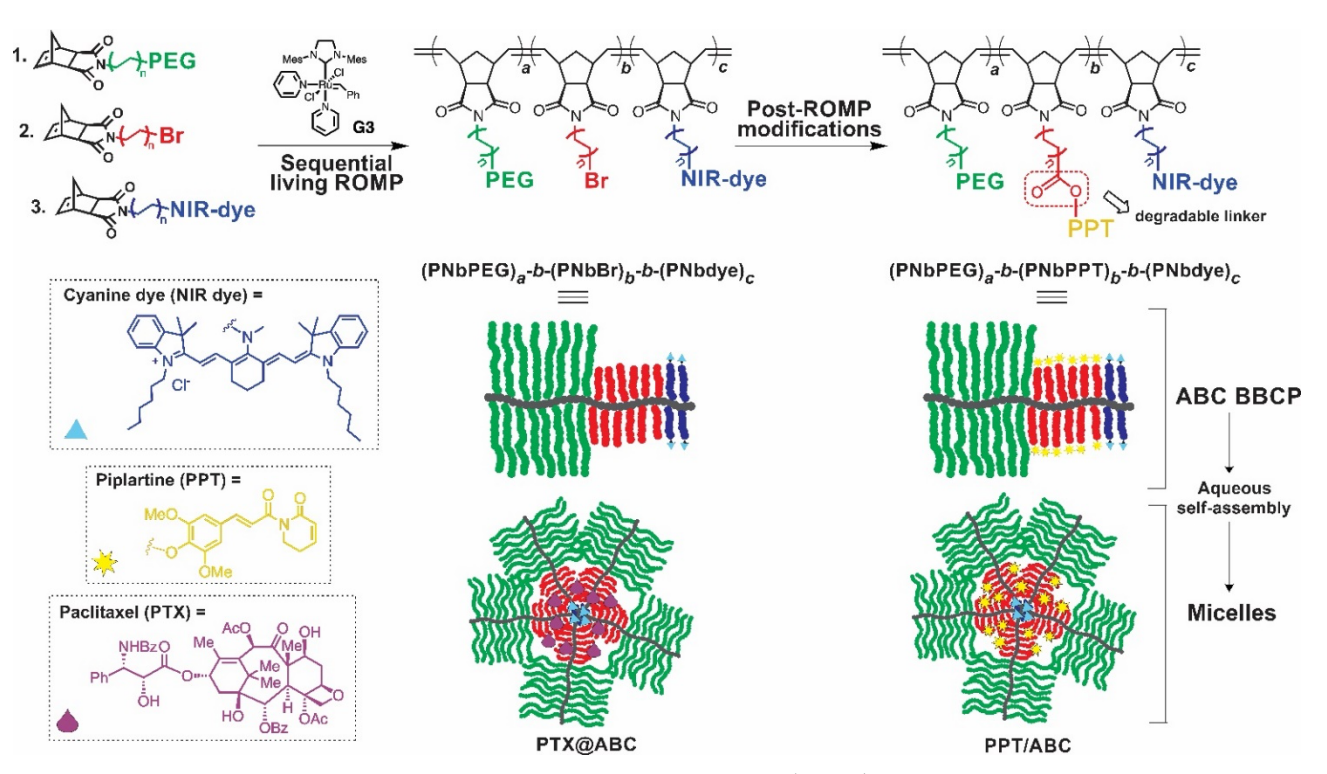


**Figure 1.** Schematic illustration for the synthesis of well-defined brush block copolymers (BBCPs) and the preparation of multifunctional fluorescent polymeric micelles from BBCPs.

unspecific interactions with blood components, to extend their circulation half-life, and to prevent fast clearance. <sup>14,15</sup> Typical nanocarrier systems that address these issues include liposomes, vesosomes, dendrimers, polymeric nanoparticles, interlocked nanomaterials, and polymeric micelles. <sup>16-23</sup>

Polymeric micelles self-assembled from amphiphilic block copolymers represent a promising platform for drug delivery applications since their size is on the nano-scale (~10-200 nm) thereby effectively and selectively penetrating tumor tissues. Polymeric micelles are fabricated rapidly from a large library of inexpensive starting materials and have tunable solubilization/dispersion properties to engineer in vivo performance. The properties of such micellar assemblies are strongly dependent on the architecture of their corresponding polymeric building blocks and, ultimately, the method employed in their synthesis. A variety of amphiphilic block copolymers with unique architectures have been investigated for drug delivery applications, including linear block copolymers and complex architectures such as brush and star-like polymers.

Living ring-opening metathesis polymerization (ROMP) is one of the most powerful methods for synthesizing well-defined amphiphilic block polymers with controlled molecular weights (MW) and low dispersities  $(\mathcal{D})$ . The sequential ROMP of norbornene-based monomers following the "grafting-through" strategy is an effective methodology for the preparation of highly branched amphiphilic brush copolymers (also known as molecular brushes or bottlebrush copolymers) with unique self-assembly, drug delivery, and imaging capabilities. This is possible due to exceptional functional group tolerance of highly active Grubbs initiators and the mild reaction conditions required.

Only a few reports have explored amphiphilic brush diblock and ABA-triblock copolymers synthesized via sequential ROMP for both drug delivery and imaging applications. 40-44 Amphiphilic poly(norbornene) diblock brush copolymers bearing a cholesterol

block and a poly(ethylene glycol) (PEG) block were studied by Lu and co-workers for the delivery of the anticancer drug doxorubicin. 42 Cheng et al. reported poly(norbornene) diblock brush co-polymerpaclitaxel conjugates with acid-sensitive cyclic acetal-based linkages, which exhibited sustained delivery of paclitaxel into cancer cells.<sup>43</sup> Random ABC brush copolymers prepared through statistical ROMP have also been reported.<sup>45</sup> Despite these advances, the preparation of well-defined amphiphilic poly(norbornene) brush triblock copolymers via sequential ROMP for drug delivery applications is very limited. 46-48 Diblock and ABC-triblock copolymers with well-defined architectures designed to self-assemble into stimuli-responsive and NIR fluorescent micelles that carry anti-cancer drugs introduces a new class of materials for nanotheranostics. Moreover, varying the composition and molecular weight will offer important insights into the structure-dependent properties and poly(norbornene) copolymers in vitro.

Natural products are an invaluable source of therapeutic agents and have driven drug discovery due to their broad spectrum of biological activity and specific molecular target. 49 Piplartine (PPT, also known as piperlongumine, Figure 1) is a naturally occurring alkaloid isolated from *Piper longum L.* (long pepper) that possesses multiple pharmacological activities such as anti-inflammatory, anxiolytic, antidepressant, anti-leishmanial, neuroprotective, antiplatelet, and antineoplastic. 50-52 PPT has been studied as a potential anticancer agent, since it exhibits cytotoxicity against different types of cancer cells, 50-51, 53-58 and presents antitumor properties in animal models. 57, <sup>59-60</sup> PPT induces cell death preferentially by elevating reactive oxygen species (ROS) levels in the intracellular medium. 55, 61-62 Additionally, ROS-independent mechanisms, such as caspase- and Baxdependent apoptosis and/or necrosis, have also been reported to be associated with PPT's anticancer activity. 53, 61 Studies on structureactivity relationship (SAR) have indicated that the  $\alpha,\beta$ -unsaturated &lactam moiety, acting as a Michael acceptor for nucleophiles available in biological environment, is the key pharmacophore essential to its cytotoxicity and ROS-generating activity, whereas the exocyclic olefin is not necessary, but important for its potency.  $^{63}$  This potential anticancer characteristic of PPT makes it an appealing compound for further development. One shortcoming of PPT, however, is its poor water solubility (26  $\mu g/mL)^{64}$  that affects its bioavailability and toxicity towards normal cells. Hence, the association of PPT to polymeric micelles offers great possibilities to overcome this drawback. Furthermore, a formulation of PPT in a suitable drug delivery system enables to protect the lactam moiety from undesired chemical transformations in the biological medium before reaching its target.

Herein, we report a micellar nanoplatform based on amphiphilic brush block copolymers (BBCPs) bearing both therapeutic and imaging functionality into a single system for nanotheranostics (Figure 1). The polymerization behavior of all new norbornenes, including their living character throughout the polymerization, are evaluated, and the ROMP conditions are optimized to tune the ratios of hydrophilic to hydrophobic chains. The well-defined AB-diblock and ABC-triblock BBCPs were synthesized through a one-pot multi-step sequential graft-through ROMP initiated by Grubbs' third generation initiator. The diblock BBCPs are composed of a hydrophilic block with poly(ethylene)glycol (PEG) pendent side-chains and a hydrophobic block containing alkyl bromide pendent side-chains designed for posterior drug functionalization. The synthesized triblock BBCP features a third polymer block containing NIR fluorescent cyanine dye moieties in its side-chains. Drug functionalization was accomplished by converting the terminal bromide groups to azides followed by the copper-free strain-promoted alkyne azide cycloaddition (SPAAC) attaching a PPT derivative via an ester linker designed to undergo enzymatic hydrolysis in the tumor microenvironment, to the polymeric nanocarrier. The BBCPs were characterized by <sup>1</sup>H NMR spectroscopy, Fourier transform infrared (FT-IR) spectroscopy, and gel-permeation chromatography (GPC). The self-assembly of these BBCPs was investigated by dynamic light scattering (DLS) and transmission electron microscopy (TEM). In addition, we also investigated the potential of these micellar assemblies to encapsulate the anticancer drug paclitaxel (PTX). The photophysical properties of the NIR fluorescent micelles in aqueous solution, as well as the micellar stability and drug release profiles from the nanosystems at different pH conditions were evaluated. The in vitro cytotoxicity and cellular uptake of the micelles were explored against a panel of different cancer and normal cell lines.

### RESULTS AND DISCUSSION

**Design and Synthesis of the Monomers.** We designed three different monomers incorporating: (i) a poly(ethylene glycol) (PEG) chain to confer water solubility and neutral surface charge to the nanoparticle, (ii) a NIR fluorescent cyanine dye to be used as imaging agent of the nanocarrier, and (iii) a primary alkyl bromide to allow easy further functionalization such as the attachment of an anticancer compound. All monomers are strained norbornene derivatives to generate the brush block copolymers (BBCPs) via ROMP. We choose *exo*-norbornene-derived imides as monomers to generate the brush block copolymers (BBCPs) because of their known fast polymerization kinetics, easy functionalization, and absence of irreversible chain-transfer, which allows for living ROMP. 65,66 The synthetic routes employed for the preparation of the three norbornene-based monomers are depicted in Schemes 1 and 2.

cis-5-Norbornene-exo-2,3-dicarboxylic anhydride (1), the common precursor for the monomers **M1** (Scheme 1), **M2** (Scheme 1), and **M3** (Scheme 2), was prepared by a Diels-Alder reaction of commercial cyclopentadiene and maleic anhydride at 200 °C followed by multiple recrystallizations (5x) from boiling toluene.<sup>67</sup> Isolation of the *exo*-isomer 1 from the *exo/endo* mixture, in 2653% yield, was essential to maintain stereochemistry throughout the steps to monomers **M1**, **M2** and **M3**. *Exo*-monomers have shown faster reaction times, higher conversion rates, and better control of ROMP compared to the *exo/endo* mixture or *endo*-form.<sup>66, 68</sup>

Scheme 1. Synthetic routes employed for the preparation of monomers Nb-PEG (M1) and Nb-Br (M2).

Macromonomer **Nb-PEG** (**M1**) was synthesized in two steps from **1** following a literature procedure<sup>69</sup> starting with the preparation of carboxylic acid **2**, which was isolated as pure compound by liquid-liquid extraction in 91% yield. Standard carbodiimideEDC-mediated esterification of **2** with commercially available poly(ethylene glycol) methyl ether ( $M_0 = 2000 \, \text{Da}$ ) in the presence of N-(3-dimethylaminopropyl)-N-ethylcarbodiimide hydrochloride (EDC•HCl) and catalytic 4-(N,N-dimethylamino)pyridine (DMAP), followed by repeated precipitations into diethyl ether, yielded the macromonomer **Nb-PEG** in 67% yield (Scheme 1). Formation of the macromonomer was confirmed by <sup>1</sup>H NMR spectroscopy (Figure SS4) and matrix-assisted laser desorption/ionization time-of-flight (MALDI-TOF) mass spectrometry (Figure SS5).

Considering that Grubbs' third generation initiator (G3) is incompatible with azides and alkynes, 70 we synthesized monomer Nb-**Br** (M2) carrying an alkyl bromide for facile conversion to azide in a post-ROMP modification step. We incorporated a ten-carbon spacer between the strained norbornene moiety and the terminal bromide to reduce steric hindrance between the growing polymer chain and the branched side-chains during ROMP and to facilitate subsequent post-ROMP functionalization. Monomer M2 was obtained in two steps from 1 (Scheme 1) through nucleophilic addition-elimination of 1 using ammonium acetate in refluxing acetic acid affording the corresponding imide 3 as a white solid in 95% yield. Subsequently, compound 3 was converted to the alkyl halide M2 in 93% yield through a N-alkylation reaction with 1,10-dibromodecane in DMF in the presence of potassium carbonate. Monomer M2 was characterized by <sup>1</sup>H and <sup>13</sup>C NMR spectroscopy (Figures S58 and S59) and high-resolution mass spectrometry (HRMS).

We designed the block copolymers BBCPs to include a short block containing a near-infrared (NIR) dye to be used as an imaging agent, allowing that allows for the direct visualization of the nanosystem inside cells. We focused on the synthesis of a dye from the tricarbocyanine family because this class of compounds has demonstrated strong fluorescence in the NIR region, high photostability, and low cytotoxicity, making them ideal NIR probes. The five reactions employed for the synthesis of the monomer **Nb-dye** (**M3**) are outlined in Scheme 2.

The preparation of the iminium salt 4 involved the Vilsmeier-Haack formylation of cyclohexanone. The Vilsmeier-Haack reagent was generated from phosphorous(V) oxychloride and N,Ndimethylformamide, which reacted in excess with cyclohexanone giving an iminium intermediate. Hydrolysis of this intermediate provided a dialdehyde, which was further transformed into iminium salt 4 by treatment with aniline. In parallel, the indolenium derivative 5 was prepared by N-alkylation of commercially available 2,3,3-trimethylindolenine with *n*-hexyl iodide in refluxing acetonitrile, followed by reflux with excess of sodium chloride to substitute the counter ion. The condensation of the quaternary ammonium salts 4 and 5 carried out under refluxing ethanol in the presence of anhydrous sodium acetate afforded the *meso*-chloro heptamethine cyanine dye 6 as a bright-green solid in 96% yield. <sup>1</sup>H and <sup>13</sup>C NMR spectroscopies (Figures S1a, S64, and S65), and HRMS unambiguously confirmed its structure.

Studies have shown that the presence of a rigid carbocyclic ring in the heptamethine chain enhances photostability and fluorescence quantum yield, as well as decreases aggregation of the dye in solution.<sup>76-77</sup> Furthermore, the meso-chlorine substituent in the cyclohexene ring provides a reactive site for the fluorophore moiety, allowing for easy functionalization with various nucleophiles. 75,78 The chlorine in the heptamethine cyanine dye 6 was displaced upon treatment with 2-methylaminoethanol to form the meso-N-methylethanolamino-substituted cyanine dye 7 as a dark-blue solid, in 61% yield. Dye 7 was characterized by <sup>1</sup>H NMR spectroscopy (Figures S1b and S66) through the presence of the new triplet signals at 4.04 and 3.93 ppm assigned to the methylene groups of the N-methylethanolamine moiety, as well as a singlet at 3.53 ppm corresponding to the hydrogens of the methyl group adjacent to the nitrogen atom. The formation of dye 7 was further confirmed by <sup>13</sup>C NMR spectroscopy (Figure S67) and by mass spectrometry (ESI-QTOF-MS) by its molecular ion peak [M]<sup>+</sup> at 662.5021 m/z (calcd. for  $C_{45}H_{64}N_3O = 662.5043 \text{ m/z}$ ).

Scheme 2. Synthetic route employed for the preparation of NIR fluorescent monomer Nb-dye (M3).

The final synthetic step shown in Scheme 2 involved the EDCmediated coupling of the carboxylic acid group of norbornene precursor 2 with the hydroxyl group of dye 7 using EDC. HCl and catalytic amounts of DMAP. Purification of the monomer containing the meso-amino derivatized cyanine dye (Nb-dye, M3) was achieved by extraction into dichloromethane and column chromatography on silica gel. The desired monomer Nb-dye has been isolated in high purity as confirmed by <sup>1</sup>H and <sup>13</sup>C NMR spectroscopies (Figures S68 and S69). The <sup>1</sup>H NMR spectrum of **Nb-dye** (Figures S1c and S68) showed the characteristic signals of the norbornene:  $\delta$  = 6.20 ppm  $(H_s)$ , 3.16 ppm  $(H_t)$ , 2.58 ppm  $(H_u)$ , 1.42-1.37 ppm  $(H_{a'})$ , and 1.10 ppm  $(H_b)$ , as well as signals assigned to the protons of the fluorophore moiety and linker. The methylene protons "H<sub>r</sub>" at 4.35 ppm shifted downfield in comparison to the corresponding ones of dye 7 (at 4.04 ppm), supporting the successful coupling reaction. Monomer Nb-dye was further characterized using mass spectrometry (ESI-QTOF-MS) by its molecular ion peak [M]<sup>+</sup> at 921.6216 m/z (calculated for  $C_{60}H_{81}N_4O_4 = 921.6252 \text{ m/z}$ ).

**Synthesis of the Clickable Bioactive Derivatives.** The preparation of the clickable derivative (**12**, BCN-PPT) of the natural product piplartine (**8**, PPT) is outlined in Scheme 3. 4-Hydroxypiplartine (**9**, 4-HOPPT) was synthesized in five steps, according to methodologies previously described by our group. S4,79 We have chosen to modify the 4-hydroxy analogue of PPT because it enables the conjugation of linkers or other moieties to its structure in a simple and

versatile way without compromising any essential residue for the PPT antitumor activity. The hydroxyl group in **9** was esterified to the carboxylic acid **10** in moderate yield (50%) through opening of glutaric anhydride in presence of catalytic amounts of DMAP in dichloromethane (DCM) under reflux.

Scheme 3. Synthesis of clickable piplartine derivative BCN-PPT (12).

The synthesis of derivative **12** was accomplished in moderate yield (43%) by the Steglich esterification of carboxylic acid **10** with commercial (1*R*,8*S*,9*S*)-bicyclo[6.1.0]non-4-yn-9-ylmethanol (BCN-OH, **11**) in the presence of the 1-hydroxybenzotriazole (HOBt) as the *N*-acylurea suppressing additive in addition to DCC and DMAP in the dark. Compound **12** was characterized by <sup>1</sup>H and <sup>13</sup>C NMR spectroscopies (Figures S73 and S74), and HRMS. The presence of a hydrolytically labile ester linker between the bioactive PPT moiety and the cyclooctyne partner was included due to its susceptibility to cleavage in the biological environment. We hypothesize that the cleavable ester linkage would undergo enzymatic hydrolysis releasing the anticancer compound 4-HOPPT (**9**) from the nanocarrier in diseased regions.

**Design and Synthesis of Amphiphilic BBCPs via ROMP.** To generate the desired amphiphilic BBCPs with precise molecular weight (MW) and unimodal MW distribution, we first screened a series of conditions to be used in the ROMP reactions. The living character of the ROMP of monomer **Nb-Br** (**M2**) and **Nb-dye** (**M3**), and their polymerization times were investigated through kinetic studies using *in situ* <sup>1</sup>H NMR spectroscopy. These kinetic experiments were conducted at constant initial monomer concentration with the initiator **G3**, in 1,2-dichloroethane (DCE) at room temperature, and monomer conversions were monitored by the disappearance of the resonance corresponding to the olefinic protons of the norbornene (at 6.3 – 6.1 ppm) and simultaneous appearance of broad olefinic signals (at 5.9 – 5.2 ppm) assigned to the brush polymer.

According to the <sup>1</sup>H NMR spectra showed in Figures S2b – S4b, as well as data in Figures S2c – S4c, all monomers polymerized quantitatively at room temperature within 45 minutes for **Nb-PEG (M1)**, 15 minutes for **Nb-Br (M2)** and 60 minutes for **Nb-dye (M3)**.

Figures S2d - S4d demonstrate the first-order kinetics and excellent molecular weight control provided by ROMP with **G3**, confirming their living character with absence of chain transfer and chain termination.

Taking into consideration the polymerization behavior of all monomers, a series of amphiphilic BBCPs (Table 1: entries 1–10) was synthesized via one-pot two- or three-step sequential ROMP of hydrophilic macromonomer **Nb-PEG** (**M1**) and hydrophobic monomers **Nb-Br** (**M2**) and **Nb-dye** (**M3**) initiated by **G3** at room temperature (Figure 2a). The effect of several parameters on the properties of the final BBCPs was investigated, including molar feed ratios of monomers to catalyst, solvent polarity, and order of block sequences. The results are summarized in Table 1. After the last block was completely formed, excess of ethyl vinyl ether (EVE) was added to the solution to quench ROMP polymerization. Polymers were isolated by multiple precipitations into diethyl ether, followed by dialysis against acetone for 48 hours.

Studies have shown the significant effect that different solvents have on the polymerization rates of ruthenium catalysts and, consequently, on the polymer characteristics. The three monomers and **G3** are soluble in DCM and DCE, which are among the preferred solvents for ROMP. As weakly polar solvents they can promote the ligand dissociation and act as non-coordinating solvents. Table 1 shows that changing the solvent from DCM ( $\epsilon$  = 9.1) to DCE ( $\epsilon$  = 10.4) has no significant effect. In all cases monomer conversions are higher than 95%, the polymers have experimental  $M_{\rm h}$  values comparable to the theoretical ones, and the dispersities (D) are in the typical ranges for living ROMP of highly branched BBCPs. Slightly lower D values were observed in DCE in comparison to DCM, which is probably related to the faster initiation observed in more polar solvents.

When a sequential hydrophilic/hydrophobic molar feed ratio of around 50:50 was employed (assuming [G3] = 1 equiv.), the resulting AB brush diblock copolymer (PNbPEG)50-b-(PNbBr)48 (BBCP7) exhibited a low dispersity, and a monomodal trace was displayed in the GPC chromatogram (Figure S5b). The number-average degree of polymerization (DP<sub>n,GPC</sub>) and number-average molecular weight  $(M_{n,GPC})$  values obtained by GPC were found to be in agreement with the theoretical ones. The small difference between the values can be attributed to different physical characteristics of the highly branched polymer studied in comparison to the linear poly(styrene) (PS) standards used for GPC calibration. <sup>1</sup>H NMR spectra (Figure S5c) confirmed that the sequential addition of monomers proceeded with their sequential incorporation into each block. The experimentally determined DP<sub>n,NMR</sub> (obtained from <sup>1</sup>H NMR spectra in Figure S77) was then used to calculate the  $M_{n,NMR}$ which was again very close to the theoretical value (Table 1). The in vitro studies were conducted using the BBCP (PNbPEG)50-b-(PNbBr)<sub>48</sub> as the representative brush diblock copolymer.

Table 1. Characterization Data of Amphiphilic Brush Block Copolymers (BBCPs) Synthesized by ROMP.

ВВСР	Туре	Experimental Composition <sup>2</sup>	Solvent	M <sub>n</sub> (kDa)			$oldsymbol{\mathcal{D}}^{arepsilon,e}$	$f_{ t philic.}^f$
Code		[Target Composition <sup>b</sup> ]	Solvent	Theor.	$\mathbf{GPC}^c$	$\mathbf{NMR}^d$		J philic.
1	AB	<b>(PNbPEG)</b> <sub>30</sub> - <i>b</i> - <b>(PNbBr)</b> <sub>59</sub> <sup>c</sup> [(PNbPEG) <sub>30</sub> - <i>b</i> -(PNbBr) <sub>70</sub> ]	DCM	95.0	90.9	N.D. <sup>g</sup>	1.45	0.752
2	AB	(PNbPEG) <sub>42</sub> -b-(PNbBr) <sub>45</sub> <sup>c</sup>	DCM	132.9	112.7	N.D.	1.56	0.847

		[(PNbPEG) <sub>50</sub> -b-(PNbBr) <sub>50</sub> ]						
3	BA	(PNbBr) <sub>40</sub> - <i>b</i> -(PNbPEG) <sub>63</sub> <sup>c</sup> [(PNbBr) <sub>30</sub> - <i>b</i> -(PNbPEG) <sub>70</sub> ]	DCM	170.7	159.4	N.D.	1.96	0.904
4	BA	<b>(PNbBr)</b> 68- <i>b</i> -(PNbPEG)52 <sup>c</sup> [(PNbBr)50- <i>b</i> -(PNbPEG)50]	DCM	132.9	143.5	N.D.	1.50	0.820
5	BA	(PNbBr) <sub>77</sub> - <i>b</i> -(PNbPEG) <sub>30</sub> <sup>c</sup> [(PNbBr) <sub>70</sub> - <i>b</i> -(PNbPEG) <sub>30</sub> ]	DCM	95.0	97.4	N.D.	1.48	0.607
6	AB	<b>(PNbPEG)</b> <sub>33</sub> - <i>b</i> -(PNbBr) <sub>76</sub> <sup>c</sup> [(PNbPEG) <sub>30</sub> - <i>b</i> -(PNbBr) <sub>70</sub> ]	DCE	95.0	104.3	N.D.	1.42	0.721
7	AB	<b>(PNbPEG)</b> <sub>50</sub> - <i>b</i> -(PNbBr) <sub>48</sub> <sup>c,d</sup> [(PNbPEG) <sub>50</sub> - <i>b</i> -(PNbBr) <sub>50</sub> ]	DCE	132.9	132.3	131.7	1.46	0.861
8	AB	<b>(PNbPEG)</b> <sub>70</sub> - <i>b</i> -(PNbBr) <sub>29</sub> <sup>c</sup> [(PNbPEG) <sub>70</sub> - <i>b</i> -(PNbBr) <sub>30</sub> ]	DCE	170.7	170.8	N.D.	1.64	0.935
9	ABC	(PNbPEG) <sub>50</sub> - <i>b</i> -(PNbBr) <sub>40</sub> - <i>b</i> -(PNbdye) <sub>12</sub> <sup>c,d</sup> [(PNbPEG) <sub>50</sub> - <i>b</i> -(PNbBr) <sub>35</sub> - <i>b</i> -(PNbdye) <sub>15</sub> ]	DCE	141.0	110.7	140.1	1.70	0.812
10	BAC	(PNbBr) <sub>17</sub> - <i>b</i> -(PNbPEG) <sub>45</sub> - <i>b</i> -(PNbdye) <sub>15</sub> <sup>c,d</sup> [(PNbBr) <sub>35</sub> - <i>b</i> -(PNbPEG) <sub>50</sub> - <i>b</i> -(PNbdye) <sub>15</sub> ]	DCE	141.0	92.4	122.9	1.90	0.834

Experimental composition is used to identify polymers throughout text.  ${}^b$ Theoretical values were calculated from the initial monomer-to-**G3** molar ratio assuming [**G3**] = 1 equiv. and complete monomer conversion. Target number-average degree of polymerization (DP<sub>n</sub>) values are subscripted after each block. Determined via GPC calibrated with poly(styrene) standards (room temperature, 0.03 M LiCl in DMF, 1 mL min<sup>-1</sup>).  ${}^d$ M<sub>n</sub> of the BBCP was estimated by first assuming complete conversion of **Nb-PEG** (**M1**) (as observed by GPC and  ${}^1$ H NMR spectroscopy after polymerization of **M1**) and then comparing the integrations of selected  ${}^1$ H NMR resonances of the hydrophobic segments to those of PEG at  $\delta$ 3.60-3.40 ppm ( ${}^-$ CH<sub>2</sub>CH<sub>2</sub> ${}^-$ ) (see Supporting Information for integrated spectra).  ${}^e$ D is the dispersity.  ${}^f$ Hydrophilic fraction based on experimental composition.  ${}^g$  N.D. = not determined.

Concomitantly, ABC and BAC brush triblock copolymers were also synthesized employing sequential copolymerization of the monomers **Nb-PEG**, **Nb-Br**, and **Nb-dye** (Figure 2a). The *D* values for ABC and BAC BBCPs were 1.70 and 1.90 (Table 1), respectively., similarly to the values of other triblock copolymers reported in the literature.80 Considering the lower dispersity obtained for (PNbPEG)<sub>50</sub>-b-(PNbBr)<sub>40</sub>-b-(PNbdye)<sub>12</sub> (BBCP9), which is an important parameter for drug delivery systems, we chose it as the representative brush triblock polymer for subsequent studies. Stepby-step analysis of the <sup>1</sup>H NMR spectra along the growing of the polymeric chain (Figure 2b) indicated the presence of typical signals of PEG chain at  $\delta$  3.72–3.48 ppm (–OC $H_2$ C $H_2$ O–), alkyl bromide chain at  $\delta$  3.37 ppm (-C $H_2$ Br), and cyanine dye moiety at  $\delta$ 7.58–6.99 ppm (aromatic H), providing evidence of the successful formation of the desired BBCP (PNbPEG)50-b-(PNbBr)40-b-(PNbdye)<sub>12</sub>. <sup>1</sup>H NMR spectroscopy also revealed high monomer conversions. For the first and second blocks, the measured  $M_{n,\mathrm{GPC}}$ were similar to the theoretically expected ones; however, the experimental  $M_{n,GPC}$  after incorporation of the third block was underestimated in comparison to the theoretical  $M_{n,theor.}$  value. We hypothesize that this is due to strong interactions between the GPC column

and the polymer, in particular the block containing the cyanine dye. Thus, the DPn of each block of the ABC polymer was estimated by assuming complete monomer conversion of **Nb-PEG** (**M1**) (as observed by  $^1$ H NMR spectroscopy) and then comparing the integrals of the peaks at 3.37 ppm ( $-CH_2$ Br of the second block) and 7.58 ppm ( $H_{aromatic}$  of the third block) to those at 3.61 ppm of PEG methylene protons (Figure S79); close agreement between the theoretical and the experimentally measured block composition was observed (Table 1).

Synthesis of Azide-Functionalized BBCPs via Bromide-Azide Substitution. Following ROMP, we carried out a post-polymerization bromide-azide exchange reaction to generate the azide-functionalized BBCP (PNbPEG)<sub>50</sub>-b-(PNbN<sub>3</sub>)<sub>40</sub>-b-(PNbdye)<sub>12</sub>, as illustrated in Figure 3a. The same methodology was employed for the synthesis of (PNbPEG)<sub>50</sub>-b-(PNbN<sub>3</sub>)<sub>48</sub>. Excess sodium azide (5 equiv. relative to bromide content) was used to ensure complete conversion of each bromide to azide. After substitution, each azide-functionalized polymer was purified via dialysis against deionized water to remove excess sodium azide and DMF.

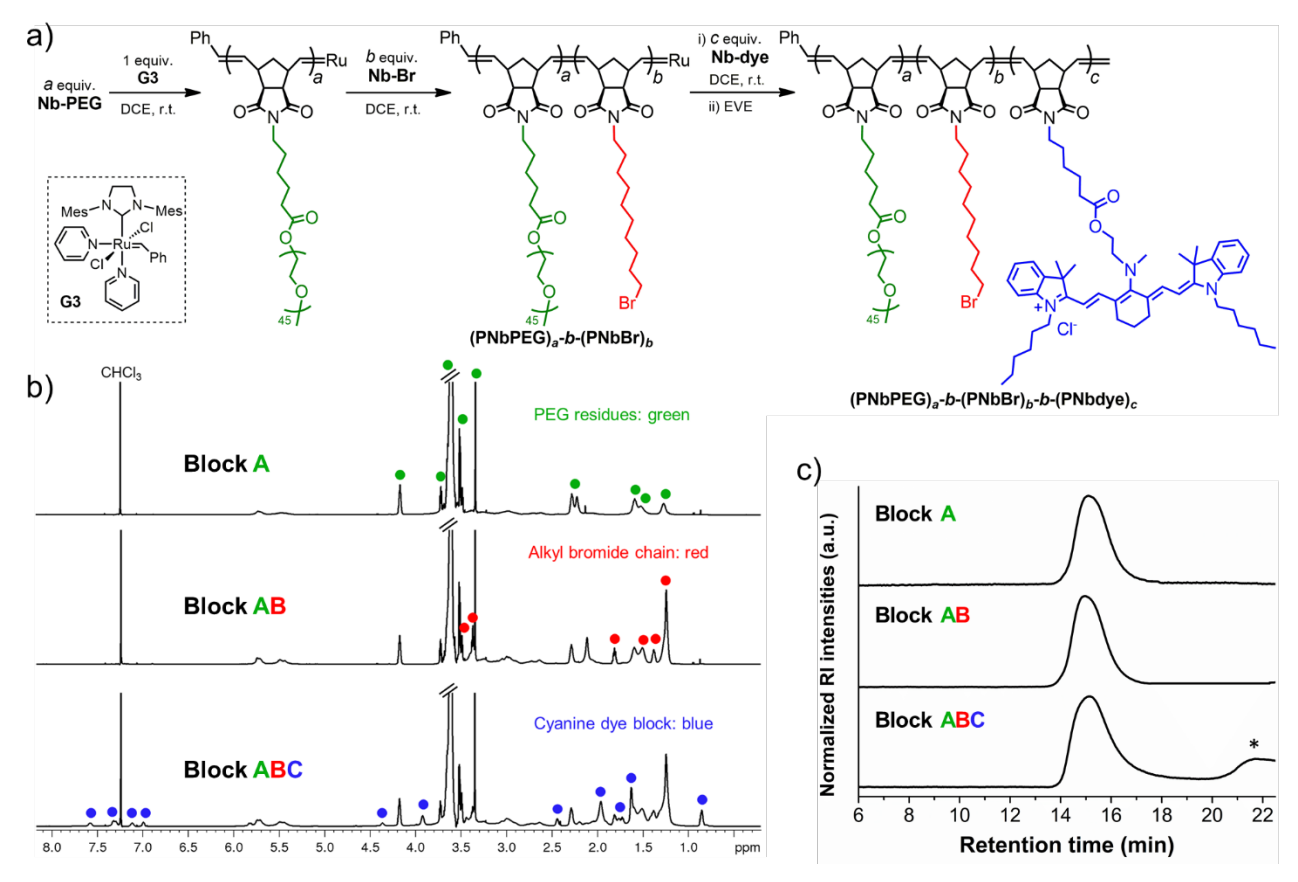


Figure 2. (a) Schematic representation of synthesis of amphiphilic BBCPs by sequential graft-through ROMP reactions. (b) <sup>1</sup>H NMR spectra of the brush homopolymer (PNbPEG)<sub>50</sub> (Block A), the diblock (PNbPEG)<sub>50</sub>-b-(PNbBr)<sub>40</sub> (Block AB) and the final BBCP (PNbPEG)<sub>50</sub>-b-(PNbBr)<sub>40</sub>-b-(PNbdye)<sub>12</sub> in CDCl<sub>3</sub> (600 MHz). Green dots correspond to PEG resonance signals, red dots correspond to the alkyl bromide chain signals and blue dots represent signals from the cyanine dye block. (c) GPC traces showing the step-by-step formation of (PNbPEG)<sub>50</sub>-b-(PNbBr)<sub>40</sub>-b-(PNbdye)<sub>12</sub>.

\* Indicates peak corresponding to small amounts of unconverted monomer.

Spectroscopic analysis (1H NMR and FT-IR) of the obtained azide-functionalized di- and triblock BBCPs was used to demonstrate the successful conversion of the pendant bromides into azides. The <sup>1</sup>H NMR spectrum of (PNbPEG)<sub>50</sub>-b-(PNbBr)<sub>40</sub>-b-(PNbdye)<sub>12</sub> (red line in Figure 3b) shows a triplet peak at  $\delta$  3.37 ppm corresponding to the methylene hydrogens adjacent to the terminal bromide ( $CH_2Br$ ). After substitution of the halides with azide groups, the signal at  $\delta$  3.37 ppm disappeared and a new triplet upfield appeared at  $\delta$  3.22 ppm (blue line in Figure 3b), which is assigned to the  $CH_2N_3$  protons of (PNbPEG)<sub>50</sub>-b-(PNbN<sub>3</sub>)<sub>40</sub>-b-(PNbdye)<sub>12</sub>. In addition, the FT-IR spectrum of the polymer after the halide-azide exchange (blue traces in Figure 3c) show a new absorption band at 2096 cm<sup>-1</sup>, which is characteristic of azide groups, confirming the successful generation of BBCP-N<sub>3</sub>. The extent of azides incorporated into the copolymer was determined via <sup>1</sup>H NMR spectroscopy (CDCl<sub>3</sub>, 600 MHz) from the comparison of peak integrations of the  $CH_2N_3$  protons at  $\delta$  3.22 ppm with the methylene protons of PEG entity at  $\delta$ 3.67–3.57 ppm (see integrated <sup>1</sup>H NMR spectra of BBCP-N<sub>3</sub> in the Supporting Information, Figure S83). The results indicate that the conversion of the pendant bromides into azides was quantitative. Similar spectroscopic analysis was also carried out for the corresponding brush diblock copolymers (PNbPEG)50-b-(PNbBr)48 and (PNbPEG)<sub>50</sub>-b-(PNbN<sub>3</sub>)<sub>48</sub> (see spectra in the Supporting Information), which showed a quantitative generation of the azidefunctionalized polymer.

Synthesis of Drug-Functionalized BBCPs via *Click* Chemistry. Copper-free strain-promoted alkyne-azide cycloaddition (SPAAC) was used to covalently attach the clickable derivative BCN-PPT (12) to the azide-functionalized BBCPs (Figure 3a). *Click* reactions are appealing for their orthogonality, mild reaction conditions, and quantitative yields. We employed SPAAC instead of the classical copper-catalyzed alkyne-azide cycloaddition (CuAAC) to avoid copper(I) contamination, which is a recognized cytotoxic element. S2-8480-83 Moreover, this copper-free reaction has proven useful for the quantitative functionalization of nanomaterials with widespread bioapplications. S5 84

Successful formation of the BBCP-PPT conjugates was verified by FT-IR spectroscopy. FT-IR spectra were acquired at different time points to monitor the SPAAC coupling (see the final FT-IR spectra of the di- and triblock conjugates in the Supporting Information). The azide asymmetric stretching at 2096 cm<sup>-1</sup>, present in the FT-IR spectrum of **(PNbPEG)**<sub>50</sub>-**b**-**(PNbN3)**<sub>40</sub>-**b**-**(PNbdye)**<sub>12</sub> (blue traces in Figure 3c), is completely absent from the final drug-functionalized BBCP **(PNbPEG)**<sub>50</sub>-**b**-**(PNbPPT)**<sub>40</sub>-**b**-**(PNbdye)**<sub>12</sub> spectrum (green traces in Figure 3c), suggesting the completion of the click reaction after 36 hours.

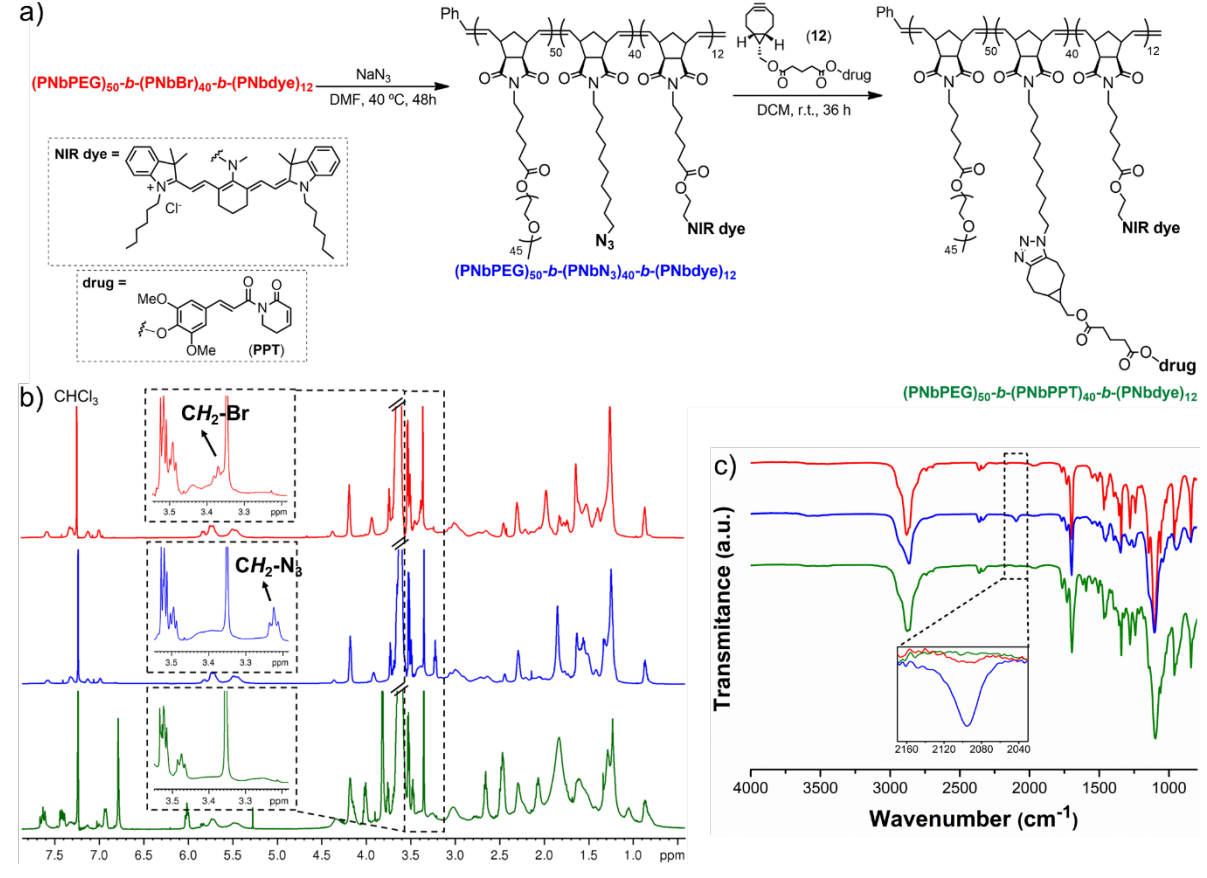


**Figure 3.** (a) Schematic representation of the synthesis of BBCP-drug conjugates via *post*-ROMP functionalization (bromide-azide substitution followed by SPAAC reaction). (b) <sup>1</sup>H NMR spectra, and (c) FT-IR spectra comparing the corresponding bromide- ((PNbPEG)<sub>50</sub>-b-(PNbBr)<sub>40</sub>-b-(PNbdye)<sub>12</sub>, red traces), azide- ((PNbPEG)<sub>50</sub>-b-(PNbN<sub>3</sub>)<sub>40</sub>-b-(PNbdye)<sub>12</sub>, blue traces) and drug-functionalized ((PNbPEG)<sub>50</sub>-b-(PNbPPT)<sub>40</sub>-b-(PNbdye)<sub>12</sub>, green traces) BBCPs.

According to <sup>1</sup>H NMR spectroscopy (green line in Figure 3b), the peak corresponding to the  $CH_2N_3$  protons at  $\delta$  3.22 ppm disappeared, also indicating consumption of the azide after 36 hours. Additionally, functionalization of the BBCP is evidenced by the presence of the peaks in the <sup>1</sup>H NMR spectrum originating from both polymer and PPT portions. The integration ratio of signal at  $\delta$ 6.02 ppm, corresponding to an olefinic proton of the PPT moiety, with respect to the signal of the methylene protons of PEG chain ( $-OCH_2CH_2O-$ ) at  $\delta$ 3.67-3.57 ppm suggest quantitative incorporation of the BCN-drug derivative into the BBCP (see Supporting Information for integrated <sup>1</sup>H NMR spectra of the BBCP-PPT conjugates).

Self-Assembly of BBCPs in Aqueous Media. An attractive feature of amphiphilic brush copolymers is their ability to behave as macrosurfactants even at very dilute concentrations. Owing to the amphiphilic nature of the synthesized BBCPs containing relatively long hydrophilic PEG side chains and short, similar length hydrophobic side chains, one can hypothesize that they spontaneously assemble in selected solvents into spherical micelles, as proposed by Rzayev and coworkers. We hypothesized that they might spontaneously assemble in selected solvents into a variety of morphologies, including spherical and cylindrical micelles. The formation of such highly ordered molecular assemblies is controlled by the balance between the hydrophilic and hydrophobic contents of the copolymer compositions, and can be predicted according to the equation developed by Discher *et al.*:86

$$f_{\text{philic}} = \sum N_{\text{philic}} m_{\text{philic}} / \sum N_{\text{philic}} m_{\text{philic}} + \sum N_{\text{phobic}} m_{\text{phobic}} \text{ eq. (1)}$$

where  $f_{\text{philic}}$  is the hydrophilic fraction,  $m_{\text{philic}}$  and  $m_{\text{phobic}}$  are the monomer mass of the hydrophilic and hydrophobic blocks that stablish the total molecular weight of the polymer, respectively, and  $N_{\text{philic}}$  and  $N_{\text{phobic}}$  are the repeating unit numbers for the hydrophilic and hydrophobic blocks, respectively. Block copolymers are expected to form spherical micelles when  $f_{\text{philic}} > 0.5$ , worm-like micelles when  $0.5 < f_{\text{philic}} < 0.4$ , vesicles for  $0.4 < f_{\text{philic}} < 0.25$ , and planar structures for  $f_{\text{philic}} < 0.25$ . The values of  $f_{\text{philic}}$  reported in Table 1 indicate that all BBCPs synthesized should self-assemble into spherical micelles.

We used nanoprecipitation followed by solvent exchange to induce assembly of the brush copolymers into micellar aggregates with a final concentration of 1 mg mL<sup>-1</sup>. Transmission electron microscopy (TEM) and dynamic light scattering (DLS) analyses were utilized to characterize the formed micelles, and the results are summarized in Table 2. Morphological investigation of the self-assembled aggregates was carried out by TEM after dropping the aqueous solution onto carbon-coated copper grids following drying at room temperature. As shown in Figure 4, TEM images confirmed that spherical nanosized micelles were obtained in all cases, suggesting that the high side chain asymmetry in the brush structure dictated their packing mode. <sup>85</sup>

The hydrodynamic diameter, size distribution, and  $\zeta$ -potential of micelles in aqueous medium were determined by DLS analysis (Figure 4 and Table 2). Results show that the average size of the AB micelles, namely blank@AB and PPT/AB micelles, is  $38 \pm 19$  nm and  $52 \pm 31$  nm, respectively, with polydispersity indices (PDI) of 0.26 and 0.35, which was smaller than their corresponding ABC micelles

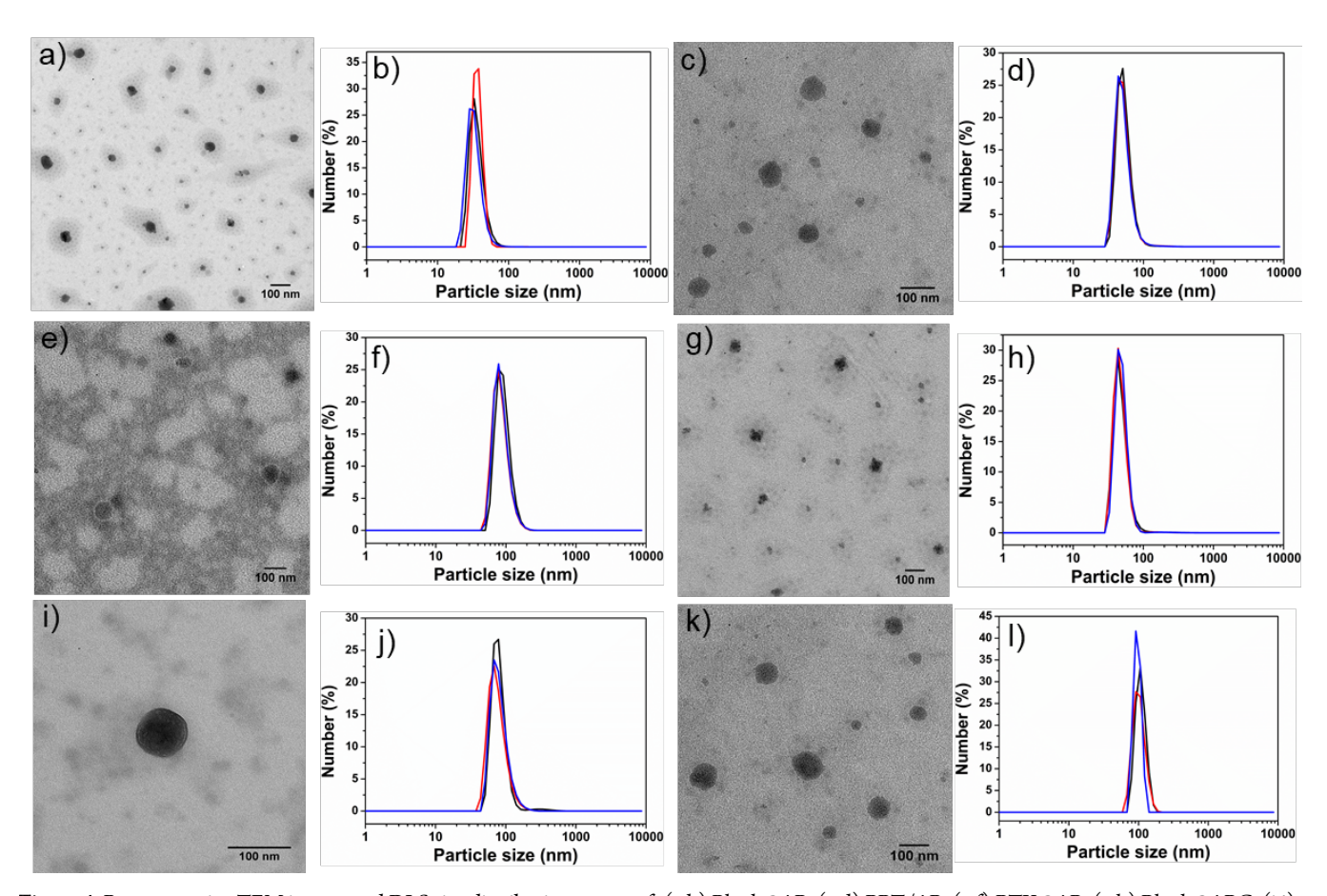


**Figure 4.** Representative TEM images and DLS size distribution curves of: (a,b) Blank@AB, (c,d) PPT/AB, (e,f) PTX@AB, (g,h) Blank@ABC, (i,j) PPT/ABC, and (k,l) PTX@ABC assembled BBCP micelles in aqueous medium. See Table 2 for more details. DLS results are presented in percentage by number and were collected in triplicate.

Table 2. Characterization data of self-assembled micelles based on BBCPs with and without paclitaxel (PTX). 3

Micelle Name	BBCP Composition	size <sup>b</sup> (nm)	$\mathbf{PDI}^{b}$	ζ-potential <sup>b</sup> (mV)	LCce(%)	<b>EE</b> <sup>d,e</sup> (%)
Blank@AB	(PNbPEG) <sub>50</sub> -b-(PNbBr) <sub>48</sub>	38 ± 19	0.26	-2.1 ± 0.8	-	-
PPT/AB	(PNbPEG) <sub>50</sub> -b-(PNbPPT) <sub>48</sub>	52 ± 31	0.35	-1.5 ± 0.5	-	-
PTX@AB	(PNbPEG) <sub>50</sub> -b-(PNbBr) <sub>48</sub>	89 ± 39	0.20	-2.1 ± 0.3	22 ± 0	93 ± 1
Blank@ABC	(PNbPEG) <sub>50</sub> -b-(PNbBr) <sub>40</sub> -b-(PNbdye) <sub>12</sub>	48 ± 30	0.39	-1.5 ± 0.7	-	-
PPT/ABC	(PNbPEG) <sub>50</sub> -b-(PNbPPT) <sub>40</sub> -b-(PNbdye) <sub>12</sub>	80 ± 42	0.28	$-0.9 \pm 0.4$	-	-
PTX@ABC	(PNbPEG) <sub>50</sub> -b-(PNbBr) <sub>40</sub> -b-(PNbdye) <sub>12</sub>	$102 \pm 53$	0.27	-1.9 ± 0.7	22 ± 0	94 ± 1

'Abbreviations: PDI = polydispersity index; LC = loading content; EE = encapsulation efficiency. In 0.01 M PBS (pH 7.4). Determined using DLS analysis. LC (wt %) = (weight of PTX in the micelles/ weight of PTX-loaded micelles) × 100. Etc (wt %) = (weight of PTX in the micelles/ weight of PTX in feed) × 100. Determined using RP-HPLC measurements. Each value is expressed as mean  $\pm$  SD from three independent measurements.

Since both AB and ABC micelles present an equal length of the hydrophilic PEG block, larger micelles were produced possibly due to the presence of the bulky cyanine dye moieties in the ABC micelles, which are expected to be in their core because of the increased hydrophobicity brought by the two C6-alkyl chains. Nanomaterials with hydrodynamic sizes of 10-200 nm can greatly reduce their

kidney clearance, capture by the macrophages, and prolong blood circulation, thereby accumulating at the tumor site through the EPR effect.<sup>9</sup>

The nanoscale size presented by the assembled micelles in aqueous solution allows them to be used as carriers for other hydrophobic anticancer compounds, like the potent drug paclitaxel (PTX). Thus,

as a demonstration of the versatility of our nanosystems, we selected blank@AB and blank@ABC micelles to encapsulate PTX to evaluate the behavior of PTX-loaded micelles in in vitro cytotoxicity studies. During micelle formation, PTX was encapsulated into the hydrophobic core. The resulting micelles (PTX@AB and PTX@ABC) were spherical in nature (Figures 4e and 4k, respectively) with average sizes of  $89 \pm 39$  nm and  $102 \pm 53$  nm, respectively (Table 2, and Figures 4f and 4l). The average sizes of PTX-loaded AB and ABC micelles are larger when compared to their corresponding blank@AB and blank@ABC micelles, suggesting successful encapsulation of PTX. Furthermore, representative TEM images showed that encapsulation did not disturb the spherical micellar structures. High loading contents (LC) of 22% were obtained, as well as high encapsulation efficiencies (93% and 94%) for PTX@AB and PTX@ABC micelles, respectively. We suggest that these results can be attributed to the presence of hydrophobic interactions between the hydrophobic anticancer drug and the hydrophobic core.

According to  $\zeta$ -potential measurements (Table 2), all micelles have a neutral surface charge, which is consistent with the dense outer PEG shell. Particles with low  $\zeta$ -potential values (-10 mV to +10mV) rapidly tend to aggregate. The steric stabilization provided by PEG chains, however, avoids micelle aggregation, as confirmed by DLS and TEM results (Figure 4).

The stability of the nanoformulations is a key parameter for their use in drug delivery applications. While nanosystems should be stable under physiological conditions to protect drugs from premature degradation and release, a stimuli responsive behavior, such as pHresponsiveness, is desirable to trigger the drug release when the nanosystem reaches the acidic tumor environment. We assessed the stability of our blank micelles under three different conditions at 37 °C: (i) 0.01 M PBS, pH 7.4, (ii) cell culture medium (RPMI) supplemented with 10% fetal bovine serum (FBS), pH 7.4, and (iii) 0.1 M acetate buffer, pH 5.5, through monitoring their sizes over a period of three days, using DLS measurements. No significant changes in the average sizes of both micelles were observed in 0.01 M PBS solution (pH 7.4) during the 72 hours (Figure 5a). Whereas, a slight increase of around 10 nm in micelles size was observed in RPMI + 10% FBS over the same period. These findings demonstrate the good colloidal stability of the micelles under physiological conditions, and the low tendency to aggregate even in a protein-enriched medium, likely due to the highly dense PEG surface coverage. The presence of PEG on the nanoparticle (NPs) surfaces is well-recognized to shield the surface from aggregation, inhibiting nonspecific interactions with serum proteins and consequently reducing macrophage uptake, leading to a prolonging of NPs systemic circulation time.9

Incubation in 0.1 M acetate buffer (pH 5.5) mimicking the mildly acidic microenvironment of tumors and endosomal/lysosomal compartments resulted in an increase of around 25 nm in the hydrodynamic size of blank@ABC micelles over 48 hours (Figure 5b). Aggregates with larger sizes and broader size distributions also emerged during this period, indicating some disassembly in the nanosytem promoted by the weakly acidic pH and, thus, a pH-responsive character of these micelles in solution.

*In Vitro* **Drug Release.** To simulate the drug release under biological conditions, the *in vitro* drug release profile of the PPT-conjugated and PTX-loaded micelles over time upon exposure to mildly acidic and physiological buffered conditions at 37 °C was investigated. As depicted in Figure 5c, PTX@AB and PTX@ABC micelles displayed minimal PTX release (*ca* 5%) at 0.01 M PBS (pH

7.4), which can be attributed to the escape of weakly interacting PTX molecules in the core of the NPs. These results corroborate those obtained in the stability studies, confirming that the self-assembled micelles are stable under physiological conditions. In turn, drug release profile at pH 5.5 reveals that 44% and 48% of PTX were released in a sustained manner from PTX@AB and PTX@ABC micelles, respectively, within 48 hours. These results clearly demonstrate that the release rates of PTX from PTX-loaded micelles are accelerated at acidic medium, presumably due to the pH-induced destabilization of the micellar structures, which leads to a faster drug leakage through the micellar scaffold.

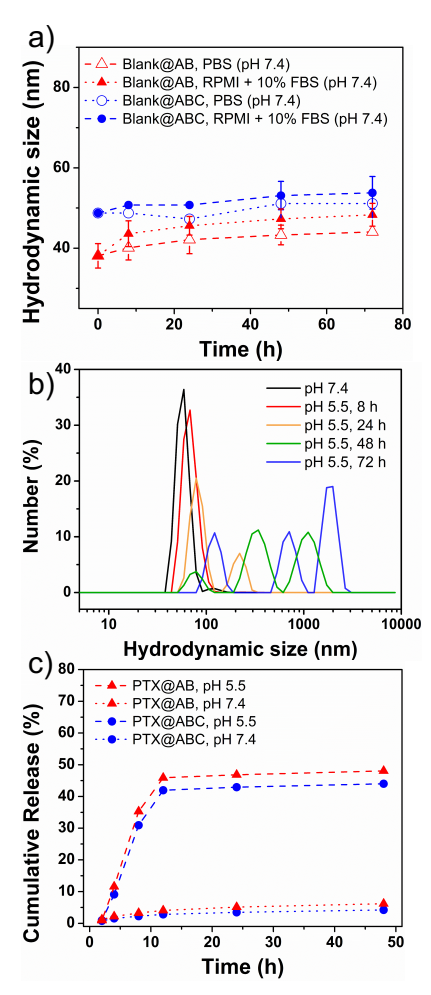


**Figure 5**. (a) Size changes of blank@AB and blank@ABC micelles over time under physiological conditions at 37 °C by DLS measurements. (b) Size changes of blank@ABC micelles over time at pH 5.5 at 37 °C by DLS measurements. (c) In vitro drug release profile of PTX from PTX@AB and PTX@ABC micelles at pH 5.5 and pH 7.4 at 37 °C during 48 h.

From an *in vivo* point of view, the low drug release at physiological pH along with the relatively elevated and sustained release of PTX at mildly acidic condition are useful features for preventing premature release in the blood stream and ensuring that the loaded drug may be effectively released inside the target tumor cells, respectively. Overall, the incomplete amount of drug released from the micelles at pH 5.5 over 48 hours suggests strong hydrophobic interactions between PTX and the hydrophobic core, and stable micelles, in agreement with previous reports about micellar drugs. <sup>87-8886-87</sup>

For PPT/AB and PPT/ABC micelles, negligible amount of PPT under acidic and physiological conditions at 37 °C over 48 hours was observed. In this case, we expect that an efficient release of PPT from these micelles in the tumor microenvironment occurs via enzymatic degradation upon cell internalization.

**Photophysical Studies.** The triblock brush copolymers contain a short block containing an NIR dye designed to easily follow cellular uptake and localization of our nanosystems. The photophysical properties of monomer **Nb-dye** (**M3**), as well as the precursor cyanine dyes **6** and **7** in different organic solvents were investigated. The complete set of NIR-UV-vis absorption and emission properties for the synthesized cyanine dyes is displayed in the Supporting Information (Figures S20 – S33, and Table S1).

Monomer **Nb-dye** displayed an absorption band with maximum absorption wavelength ( $\lambda_{max}$ ) at 709-727 nm depending on the solvent (Figures S34 – S40, and Table S1). Also, high molar extinction coefficients ( $\epsilon$ ) were obtained for this monomer, ranging from 5 ×  $10^4\,M^{-1}\,cm^{-1}$  in THF to  $14\times10^4\,M^{-1}\,cm^{-1}$  in DCM. Contrary to some reported cyanine dyes that are known to aggregate in solution through plane-to-plane stacking forming H-type aggregates, or through head-to-tail arrangement leading to J-type aggregates, our results demonstrate no tendency of monomer **Nb-dye** to form J-type aggregates and only limited amounts of H-type aggregates can be found in bands at shorter wavelength region (hypsochromic shift) in most of the studied solvents. Similar behavior was also recently reported by us for a similar cyanine dye. 73

The emission spectrum of monomer **Nb-dye** in the NIR region shows a maximum emission peak around 800 nm in all solvents. As expected, monomer **Nb-dye** displayed Stokes shifts of ~ 90 nm that are much larger than the typical Stokes shifts of other fluorescent dyes, like its precursor *meso*-chloro cyanine dye **6** (Table S1). The large Stokes shift observed in amino-substituted cyanine dyes is frequently assigned to an intramolecular charge transfer (ICT) between donor and acceptor in the dyes, although clear experimental evidence of this photophysical feature has not been fully reported. <sup>89-9088-89</sup> Notwithstanding, this makes it less susceptible to self-quenching and a promising candidate to be used as the fluorophore in drug delivery systems.

The NIR-UV-vis absorption and emission spectra of the cyanine dye-functionalized BBCPs in DCM and dimethylsulfoxide (DMSO) displayed the same maxima locations (absorption and emission) and band shape as the **Nb-dye**, confirming the successful introduction of the cyanine moiety into the polymers without interfering in its optical properties (Figures S41 – S46, and Table S1). The absorption and emission spectra of the micelles, in 0.01 M PBS buffer at pH 7.4 (Figures S47 – S47), demonstrate successful preservation of optical characteristics of monomeric dye (**Nb-dye**) in aqueous conditions. Interestingly, NIR-UV-vis absorption spectrum of blank@ABC micelles exhibited low tendency for H-aggregation in buffered aqueous solution (Figure S47).

**Cellular Uptake Assay.** Confocal laser scanning microscopy (CLSM) was employed to investigate the cellular uptake of NIR fluorescent blank@ABC and PPT/ABC micelles in tumor and normal

cells. The nuclei of the cells were stained with Hoechst 33382 (presented in blue), whereas Alexa Fluor 555 Phalloidin allowed to label the cytoskeleton (presented in red) through the binding of phalloidin to F-actin. Green color was chosen in the confocal software for representing the fluorescence of the NIR-dye present in the blank@ABC and the PPT/ABC micelles.

As shown in Figure 6, after eight hours of incubation with blank@ABC micelles, treated MCF-7 cell line showed some intensity of NIR fluorescence, as represented by green color, indicating that micelles were quickly internalized into the cell membrane and diffused in both cytoplasm and the cell nuclei. Using the same settings during acquisition of images it can be observed that the intensity of fluorescence signal of blank@ABC micelles inside cells substantially increased with prolonged incubation time (24h).

The cellular uptake of PPT/ABC micelles was also investigated in MCF10A, MCF-7 and PC3 cells. In Figure 7a it can be noticed that MCF-7 breast cancer cells and PC3 prostate cancer cells presented stronger intracellular fluorescence signal than the normal breast cells MCF10A after 24 hours. Indeed, the mean fluorescence intensity of green color analyzed by Image J software (Figure 7b) confirms that PPT/ABC micelles were uptaken more efficiently by cancer cells (MCF-7 and PC3) than by healthy cells (MCF10A).

To further support the cellular uptake of both blank@ABC and PPT/ABC micelles, orthogonal projections of CLSM images showed in Figures 6 and 7a were built (Figures S108-S111). The images confirm the previous findings, indicating the presence of green fluorescence from micelles inside cell nuclei and cytoplasm.

CLSM was used only as a supporting tool to demonstrate cell uptake for this proof-of-concept study. Due to restrictions of the confocal laser scanning microscopy instrument, an excitation laser of 633 nm for cyanine dye channel was used, and its fluorescence was detected at 661-759 nm, which are significantly far from the maxima absorption and fluorescence wavelengths in their spectra (Figures S47 – S49). As consequence, a weak fluorescence intensity of both micelles was observed, in contrast to the intense fluorescence in their emission spectra. Nevertheless, the results indicate the potential of our nanosystems as probes for biomedical imaging.

*In Vitro* Cytotoxicity Assay. The cytotoxicity of the blank, PPT-conjugated and PTX-loaded micelles was assessed by colorimetric assay using the Cell Counting Kit-8 (CCK-8 assay), after incubation of cells for 48 hours with varied concentrations of each compound. The *in vitro* experiments were performed using cultured monolayers of human healthy and cancer cell lines: MCF-7 (breast adenocarcinoma), PC3 (prostate adenocarcinoma), MCF10A (normal breast cells), PNT2 (normal prostate cells), and MDA-MB-231 (triple negative breast cancer cells).

Blank@AB and blank@ABC micelles displayed no significant cytotoxicity in the different cell lines over the range of concentrations analyzed, with cell viabilities above 80% after 48 hours treatment (Figures 8 and S88, respectively), even when the concentration of the micelles was as high as 1 mg mL<sup>-1</sup>. These data are encouraging because they suggest an inherent non-toxicity and good biocompatibility of the blank micelles towards a panel of different cell lines.

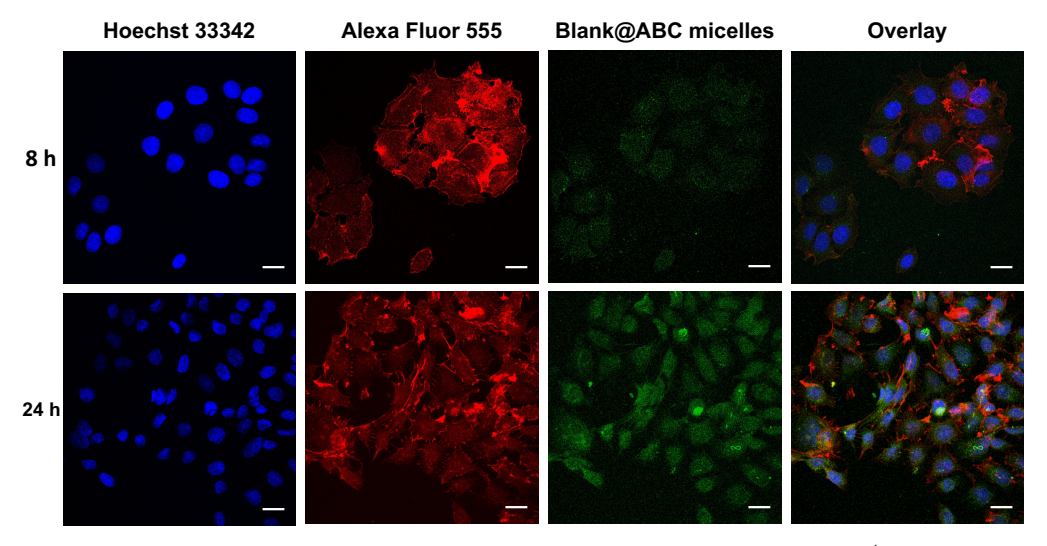


**Figure 6.** Confocal laser scanning microscopy images of MCF-7 cells showing the subcellular localization of nuclei (Hoechst 33342 stained, blue channel), F-actin cytoskeleton (Alexa Fluor 555 Phalloidin, red channel) and blank@ABC micelles (green channel). The cells were incubated with blank@ABC micelles for 8 hours and 24 hours at 37 °C. Scale bars represent 20  $\mu$ m.

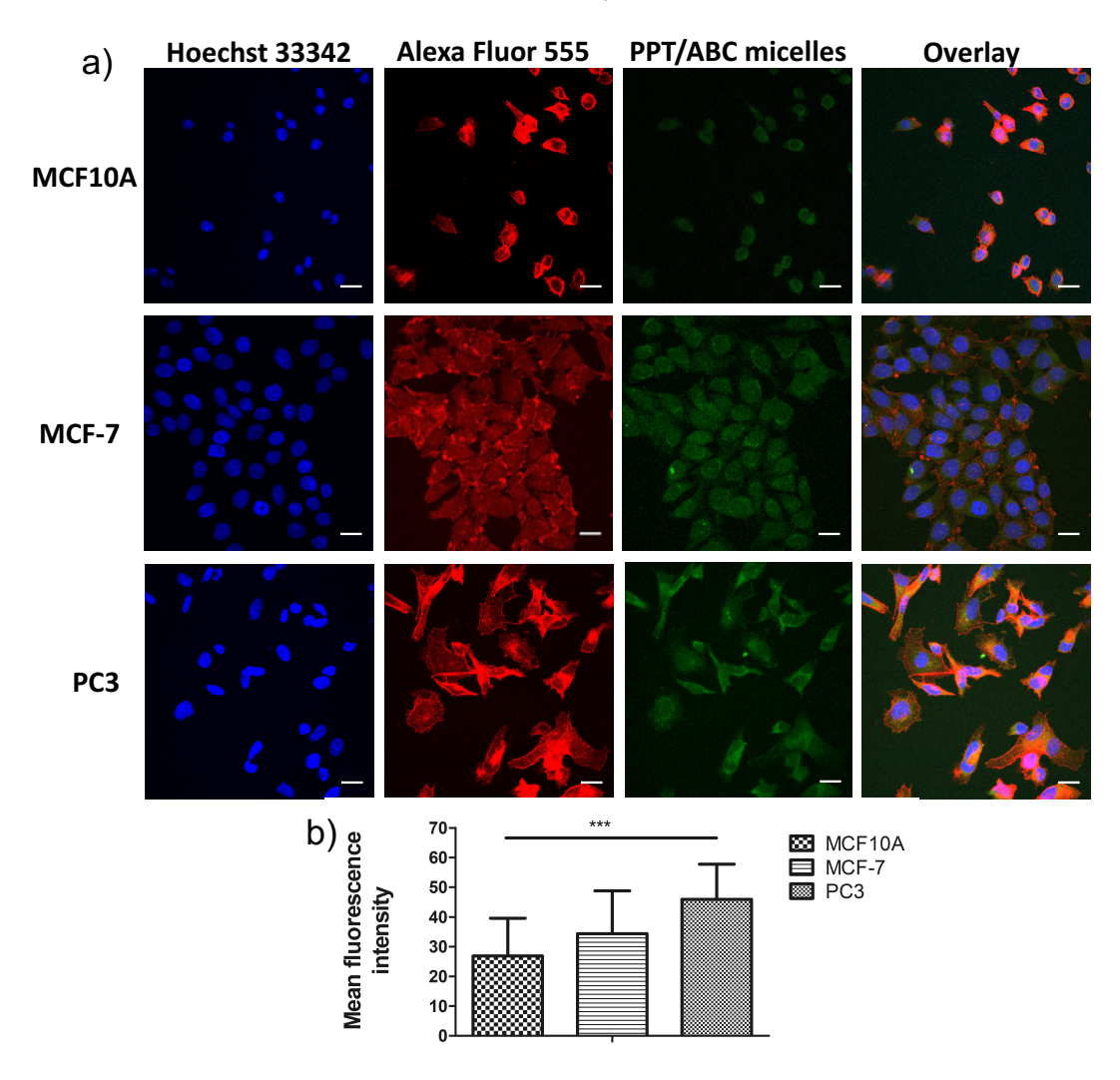
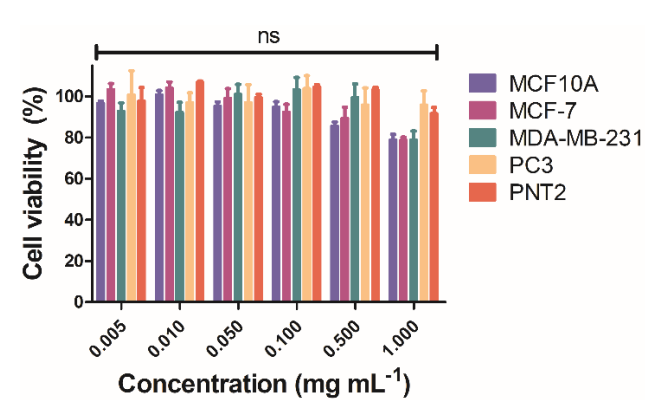


Figure 7. (a) Confocal laser scanning microscopy images of MCF10A, MCF-7, and PC3 cells showing the subcellular localization of nuclei (Hoechst 33342 stained, blue channel), F-actin cytoskeleton (Alexa Fluor 555 Phalloidin, red channel) and PPT/ABC micelles (green channel). The cells were incubated with PPT/ABC micelles for 24 hours at 37 °C. Scale bars represent 20  $\mu$ m. (b) Mean fluorescence intensity of green color between different groups (calculated using Image J software). One-way ANOVA was performed for group comparison and significant differences were observed among all groups (\*\*\*\*p<0.05). Data are reported as mean  $\pm$  SD.



**Figure 8.** Cell viability of different cell lines treated with blank@ABC micelles at varying concentrations for 48 hours. Data are presented as mean ± SD of two independent experiments, each one performed in triplicate. One-way ANOVA followed by Tukey's post-hoc test did not reveal a significant difference (ns) for all comparisons (p>0.05).

PPT-conjugated and PTX-loaded micelles exhibited similar high cytotoxicity as the free piplartine (PPT) and paclitaxel (PTX) against cancer cells (Table 3). We also used the cytotoxic 4-hydroxypiplartine (4-HOPPT) as positive control, which after enzymatic hydrolysis should be released from the PPT-conjugated micelles. PPT/AB and PPT/ABC micelles displayed IC<sub>50</sub> values of  $3.0 \pm 0.1$  $\mu M$  and 5.5  $\pm$  0.7  $\mu M$ , respectively, on PC3 cells, which are slightly lower than the IC<sub>50</sub> value of free PPT  $(7.2 \pm 0.4 \,\mu\text{M})$ . No significant difference in IC50 values were observed for the two micelles and PPT against MCF-7 cells. These PPT-conjugated micelles were less cytotoxic than the pristine drug on normal MCF10A cells, i.e. free PPT destroyed these normal cells unselectively, while treatment with the micelles could maintain higher cell viability after 48 hours, as demonstrated by the higher S.I. values for the micelles. Similar outcomes were also obtained for the PTX-loaded micelles. While no significant decrease in cytotoxicity was observed for PTX@AB and PTX@ABC micelles in comparison to PTX against MCF-7 cells, micelles were more selective than the free drug against breast cancer cells. These comparative studies not only strongly suggest that micelles are effective to penetrate cell membrane and perform controlled drug release triggered by the tumor-specific environment, but also show the potential application of micelles from BBCPs as selective anticancer drug nanocarriers both via drug conjugation and encapsulation. Our nanosystems demonstrated the desirable features to minimize the side-effects of two cytotoxic compounds while slightly increased the maximal therapeutic effect for targeted diseases. Moreover, the selectivity index is expected to be amplified in in vivo studies due to the addition of the EPR effect and higher tumor accumulation of the nanosystems.

Table 3. *In vitro* cytotoxic activities of studied micelles and free anticancer compounds against different human cell lines<sup>a</sup> using CCK-8 assay.

Sample	IC <sub>50</sub> (μM) <sup>b</sup>				
Sample	MCF-7	MCF10A	PC3	S.I. <sup>c</sup>	
PPT	$5.3 \pm 0.4$	$5.5 \pm 0.1$	$7.2 \pm 0.4$	1.0	
4-HOPPT	7.3 ±1.1	$5.6 \pm 0.0$	$5.4 \pm 0.1$	0.7	
AB/PPT	$5.5 \pm 0.2$	$7.9 \pm 0.6$	$3.0 \pm 0.1$	1.4	
ABC/PPT	$6.3 \pm 0.0$	12.1 ± 0.8	$5.5 \pm 0.7$	1.9	
PTX	$2.5 \pm 0.0$	$3.3 \pm 0.5$	N.D.	1.3	
PTX@AB	$2.7 \pm 1.3$	$5.2 \pm 0.9$	N.D.	1.9	
PTX@AB C	2.6 ± 1.1	$6.7 \pm 0.6$	N.D.	2.6	

 $^a$ MCF-7: breast cancer cell line; MCF10A: normal breast cell line; PC3: prostate cancer cell line.  $^b$ The half maximum inhibitory concentration (IC<sub>50</sub>) values are the mean  $\pm$  SD from two independent experiments performed in triplicate per plate.  $^c$  SI: selectivity index defined as the ratio between the IC<sub>50</sub> value in the normal cell line MCF10A to the IC<sub>50</sub> value in the cancer cell line MCF-7: SI= IC<sub>50</sub> (MCF10A)/ IC<sub>50</sub> (MCF-7). ND: not determined.

#### **CONCLUSIONS**

In summary, We have demonstrated the successful synthesis, characterization, and self-assembly of multifunctional amphiphilic poly(norbornene) brush block copolymers for drug delivery and biological imaging was demonstrated. A detailed investigation of the ROMP behavior of all norbornene-functionalized monomers initiated by Grubbs' third generation initiator, including their livingness and polymerization times, was carried out. Using optimized polymerization conditions and a combination of one-pot sequential grafting-through ROMP of the norbornene-based monomers, followed by halide-azide substitution and copper-free SPAAC, well-defined amphiphilic brush block copolymers containing hydrophilic PEG, the anticancer compound piplartine and/or a NIR fluorescent cyanine dye in their side-chains were obtained. The aqueous self-assembly behavior of these amphiphilic brush block copolymers was investigated, which revealed spherical micelles with nanoscale sizes with the capacity to efficiently encapsulate the anticancer drug paclitaxel. The amphiphilic brush block copolymers were self-assembled into spherical micelles in aqueous medium, using a nanoprecipitation method and solvent exchange, with particle sizes ranging from 30 to 110 nm and low polydispersities. The efficient encapsulation of paclitaxel into the micelles during self-assembly was also achieved evaluated and high loading content and encapsulation efficacy were obtained. The micelles demonstrated excellent preservation of photophysical properties of monomeric dye (Nb-dye), such as large Stokes shifts and strong fluorescence in the NIR region, as well as exhibited high colloidal stability at physiological conditions and a pH-induced destabilization under mildly acidic condition. Release studies at 37  $^{\circ}$ C over 48 hours showed that 40-50% of PTX was released in a controlled manner at pH 5.5, while less than 10% minimal amount of the drug was released at pH 7.4, suggesting a pH-responsive behavior. In vitro assays show the low toxicity of blank micelles even at high concentrations of 1 mg mL<sup>-1</sup>. In turn, the micelles containing attached piplartine or encapsulated paclitaxel in their structures exhibited similar cytotoxicity but enhanced selectivity towards human cancer cells (MCF-7 and PC3) in comparison to the free drugs. CSLM images unambiguously showed that both blank@ABC and PPT/ABC micelles were efficiently internalized into the cancer cells. Overall, the results obtained with show that our

micelles make them are promising nanosystems for nanotheranostics and encouraging for further evaluation of *in vivo* anticancer activity in systemic delivery taking advantage of the EPR effect. Further research in our group will also is exploringe the design of novel stimuli-responsive linkers, the attachment of brush block copolymers BBCPs via *Click* chemistry with of other functionalities (e.g., targeting moieties), incorporation of degradable units within the brush copolymer backbone, as well as and the encapsulation of other bioactive compounds, providing access to new multifunctional brush block copolymers with potential for nanomedicine applications.

### **ASSOCIATED CONTENT**

## Supporting Information.

The Supporting Information is available free of charge via the Internet at http://pubs.acs.org.

Materials and methods; Synthetic procedures; Structural characterization (<sup>1</sup>H NMR, <sup>13</sup>C NMR, FT-IR, and MALDI-TOF spectra) of monomers, precursors, anticancer derivatives, and polymers; General experiments; ROMP kinetic experiments; GPC traces for all the synthesized BBCPs; NIR-UV-vis absorption and fluorescence emission spectra of cyanine dye-related compounds; and dose-response curves obtained in cell viability assays; and orthogonal projections of CLSM images.

# **AUTHOR INFORMATION**

### **Corresponding Authors**

\*Marcus Weck – Molecular Design Institute and Department of Chemistry, New York University, 100 Washington Square East, New York, NY 10003, United States; E-mail: marcus.weck@nyu.edu

\*Catia Ornelas – Institute of Chemistry, University of Campinas (UNICAMP), P.O. Box 6154, CEP 13083-970, Campinas, SP, Brazil; E-mail: catiaornelas@catiaornelaslab.com

# **ORCID**

C.B. Braga: 0000-0003-1800-386X R.A. Pilli: 0000-0002-5919-7763 C. Ornelas: 0000-0001-8020-9776 M. Weck: 0000-0002-6486-4268

Notes

The authors declare no competing financial interest.

# **ACKNOWLEDGMENTS**

The authors gratefully acknowledge Sao Paulo Research Foundation (FAPESP) (fellowships #2017/06146-8 and #2018/24020-4 for C.B.B. and research grants #2021/00555-9 for C.O. and #2019/13104-5 for R.A.P.), National Council for Scientific and Technological Development (CNPq) (307403/2018-1 for C.O. and 307500/2015-2 for R.A.P.), and the Obesity and Comorbidities Research Center (OCRC) (2013/07607-8). This study was financed in part by the Coordination for the Improvement of Higher Education Personnel (CAPES). We also acknowledge the National Science Foundation (CHE-0958457) for the purchase of the MALDI-ToF MS, and the NHI for the purchase of the Avance III-600 CPTCI-cryoprobe head (S10 grant, OD016343). We also thank the access to the confocal microscope and assistance provided by the National Institute of Science and Technology on Photonics Applied to Cell Biology (INFABIC) at the State University of Campinas; INFABIC is cofunded by Fundação de Amparo a Pesquisa do Estado de São Paulo (FAPESP) (08/57906-3) and Conselho Nacional de Desenvolvimento Cientifico e Tecnológico (CNPq) (573913/2008-0).

### **REFERENCES**

- 1. Chabner, B. A.; Roberts, T. G. Timeline Chemotherapy and the War on Cancer. *Nat. Rev. Cancer* **2005**, 5, 65-72.
- 2. DeVita, V. T.; Chu, E. A History of Cancer Chemotherapy. *Cancer Res.* **2008**, *68*, 8643-8653.
- 3. Narvekar, M.; Xue, H. Y.; Eoh, J. Y.; Wong, H. L. Nanocarrier for Poorly Water-Soluble Anticancer Drugs Barriers of Translation and Solutions. *AAPS PharmSciTech* **2014**, *15*, 822-833.
- 4. Gala, U. H.; Miller, D. A.; Williams, R. O., III. Harnessing the Therapeutic Potential of Anticancer Drugs Through Amorphous Solid Dispersions. *Biochim. Biophys. Acta Rev. Cancer* **2020**, *1873*, 188319.
- 5. Peer, D.; Karp, J. M.; Hong, S.; FaroKHzad, O. C.; Margalit, R.; Langer, R. Nanocarriers as an Emerging Platform for Cancer Therapy. *Nat. Nanotechnol.* **2007**, *2*, 751-760.
- 6. Wicki, A.; Witzigmann, D.; Balasubramanian, V.; Huwyler, J. Nanomedicine in Cancer Therapy: Challenges, Opportunities, and Clinical Applications. *J. Control. Release* **2015**, *200*, 138-157.
- 7. Arranja, A. G.; Pathak, V.; Lammers, T.; Shi, Y. Tumor-Targeted Nanomedicines for Cancer Theranostics. *Pharmacol. Res.* **2017**, *115*, 87-95.
- 8. Bjornmalm, M.; Thurecht, K. J.; Michael, M.; Scott, A. M.; Caruso, F. Bridging Bio-Nano Science and Cancer Nanomedicine. *ACS Nano* **2017**, *11*, 9594-9613.
- 9. Shi, J.; Kantoff, P. W.; Wooster, R.; Farokhzad, O. C. Cancer Nanomedicine: Progress, Challenges and Opportunities. *Nat. Rev. Cancer* **2017**, *17*, 20-37.
- 10. Barenholz, Y. Doxil(R) The First FDA-Approved Nano-Drug: Lessons Learned. *J. Control. Release* **2012**, *160*, 117-134.
- 11. Min, Y.; Caster, J. M.; Eblan, M. J.; Wang, A. Z. Clinical Translation of Nanomedicine. *Chem. Rev.* **2015**, *115*, 11147-11190.
- 12. Tran, S.; DeGiovanni, P. J.; Piel, B.; Rai, P. Cancer Nanomedicine: A Review of Recent Success in Drug Delivery. *Clin. Transl. Med.* **2017**, *6*, 44.
- 13. Anselmo, A. C.; Mitragotri, S. Nanoparticles in the Clinic: An Update. *Bioeng. Transl. Med.* **2019**, *4*, e10143.
- 14. Sun, T.; Zhang, Y. S.; Pang, B.; Hyun, D. C.; Yang, M.; Xia, Y. Engineered Nanoparticles for Drug Delivery in Cancer Therapy. *Angew. Chem. Int. Ed.* **2014**, *53*, 12320-12364.
- 15. Tee, J. K.; Yip, L. X.; Tan, E. S.; Santitewagun, S.; Prasath, A.; Ke, P. C.; Ho, H. K.; Leong, D. T. Nanoparticles' Interactions with Vasculature in Diseases. *Chem. Soc. Rev.* **2019**, *48*, 5381-5407.
- 16. Astruc, D.; Boisselier, E.; Ornelas, C. Dendrimers Designed for Functions: From Physical, Photophysical, and Supramolecular Properties to Applications in Sensing, Catalysis, Molecular Electronics, Photonics, and Nanomedicine. *Chem. Rev.* **2010**, *110*, 1857-1959.
- 17. Kannan, R. M.; Nance, E.; Kannan, S.; Tomalia, D. A. Emerging Concepts in Dendrimer-Based Nanomedicine: From Design Principles to Clinical Applications. *J. Intern. Med.* **2014**, *276*, 579-617.
- 18. Pattni, B. S.; Chupin, V. V.; Torchilin, V. P. New Developments in Liposomal Drug Delivery. *Chem. Rev.* **2015**, *115*, 10938-10966.
- 19. Grimaldi, N.; Andrade, F.; Segovia, N.; Ferrer-Tasies, L.; Sala, S.; Veciana, J.; Ventosa, N. Lipid-Based Nanovesicles for Nanomedicine. *Chem. Soc. Rev.* **2016**, *45*, 6520-6545.
- 20. Ornelas, C. Brief Timelapse on Dendrimer Chemistry: Advances, Limitations, and Expectations. *Macromol. Chem. Phys.* **2016**, *217*, 149-174.
- 21. Chen, G. Y.; Roy, I.; Yang, C. H.; Prasad, P. N. Nanochemistry and Nanomedicine for Nanoparticle-based Diagnostics and Therapy. *Chem. Rev.* **2016**, *116*, 2826-2885.
- 22. Pick, H.; Alves, A. C.; Vogel, H. Single-Vesicle Assays Using Liposomes and Cell-Derived Vesicles: From Modeling Complex Membrane Processes to Synthetic Biology and Biomedical Applications. *Chem. Rev.* **2018**. *118*. 8598-8654.
- 23. Ornelas-Megiatto, C.; Becher, T. B.; Megiatto, J. D. Interlocked Systems in Nanomedicine. *Curr. Top. Med. Chem.* **2015**, *15*, 1236-1256.
- 24. Owen, S. C.; Chan, D. P. Y.; Shoichet, M. S. Polymeric Micelle Stability. *Nano Today* **2012**, *7*, 53-65.

- 25. Ghezzi, M.; Pescina, S.; Padula, C.; Santi, P.; Del Favero, E.; Cantu, L.; Nicoli, S. Polymeric Micelles in Drug Delivery: An Insight of the Techniques for Their Characterization and Assessment in Biorelevant Conditions. *J. Control. Release* **2021**, *332*, 312-336.
- 26. Pepic, I.; Lovric, J.; Filipovic-Grcic, J. How Do Polymeric Micelles Cross Epithelial Barriers? *Eur. J. Pharm. Sci.* **2013**, *50*, 42-55.
- 27. Barnes, J. C.; Bruno, P. M.; Nguyen, H. V.; Liao, L.; Liu, J.; Hemann, M. T.; Johnson, J. A. Using an RNAi Signature Assay To Guide the Design of Three-Drug-Conjugated Nanoparticles with Validated Mechanisms, *In Vivo* Efficacy, and Low Toxicity. *J. Am. Chem. Soc.* **2016**, *138*, 12494-12501.
- 28. Cabral, H.; Miyata, K.; Osada, K.; Kataoka, K. Block Copolymer Micelles in Nanomedicine Applications. *Chem. Rev.* **2018**, *118*, 6844-6892.
- 29. Varlas, S.; Lawrenson, S. B.; Arkinstall, L. A.; O'Reilly, R. K.; Foster, J. C. Self-Assembled Nanostructures from Amphiphilic Block Copolymers Prepared via Ring-Opening Metathesis Polymerization (ROMP). *Prog. Polym. Sci.* **2020**, *107*, 101278.
- 30. Dag, A.; Cakilkaya, E.; Omurtag Ozgen, P. S.; Atasoy, S.; Yigit Erdem, G.; Cetin, B.; Cavus Kokuroglu, A.; Gurek, A. G. Phthalocyanine-Conjugated Glyconanoparticles for Chemo-photodynamic Combination Therapy. *Biomacromolecules* **2021**, *22*, 1555-1567.
- 31. Bielawski, C. W.; Grubbs, R. H. Living Ring-Opening Metathesis Polymerization. *Prog. Polym. Sci.* **2007**, *32*, 1-29.
- 32. Xia, Y.; Kornfield, J. A.; Grubbs, R. H. Efficient Synthesis of Narrowly Dispersed Brush Polymers via Living Ring-Opening Metathesis Polymerization of Macromonomers. *Macromolecules* **2009**, *42*, 3761-3766.
- 33. Nomura, K.; Abdellatif, M. M. Precise Synthesis of Polymers Containing Functional End Groups by Living Ring-Opening Metathesis Polymerization (ROMP): Efficient Tools for Synthesis of Block/Graft Copolymers. *Polymer* **2010**, *51*, 1861-1881.
- 34. Verduzco, R.; Li, X.; Pesek, S. L.; Stein, G. E. Structure, Function, Self-Assembly, and Applications of Bottlebrush Copolymers. *Chem. Soc. Rev.* **2015**, *44*, 2405-2420.
- 35. Pelras, T.; Mahon, C. S.; Mullner, M. Synthesis and Applications of Compartmentalised Molecular Polymer Brushes. *Angew. Chem. Int. Ed.* **2018**, *57*, 6982-6994.
- 36. Xie, G.; Martinez, M. R.; Olszewski, M.; Sheiko, S. S.; Matyjaszewski, K. Molecular Bottlebrushes as Novel Materials. *Biomacromolecules* **2019**, *20*, 27-54.
- 37. Ahmed, E.; Womble, C. T.; Weck, M. Synthesis and Aqueous Self-Assembly of ABCD Bottlebrush Block Copolymers. *Macromolecules* **2020**, *53*, 9018-9025.
- 38. Kuepfert, M.; Ahmed, E.; Weck, M. Self-Assembled Thermoresponsive Molecular Brushes as Nanoreactors for Asymmetric Aldol Addition in Water. *Macromolecules* **2021**, *54*, 3845-3853.
- 39. Love, J. A.; Morgan, J. P.; Trnka, T. M.; Grubbs, R. H. A Practical and Highly Active Ruthenium-Based Catalyst That Effects the Cross Metathesis of Acrylonitrile. *Angew. Chem. Int. Ed.* **2002**, *41*, 4035-4037.
- 40. Saha, B.; Choudhury, N.; Seal, S.; Ruidas, B.; De, P. Aromatic Nitrogen Mustard-Based Autofluorescent Amphiphilic Brush Copolymer as pH-Responsive Drug Delivery Vehicle. *Biomacromolecules* **2019**, *20*, 546-557.
- 41. Shao, Y.; Jia, Y. G.; Shi, C.; Luo, J.; Zhu, X. X. Block and Random Copolymers Bearing Cholic Acid and Oligo(ethylene glycol) Pendant Groups: Aggregation, Thermosensitivity, and Drug Loading. *Biomacromolecules* **2014**, *15*, 1837-1844.
- 42. Tran, T. H.; Nguyen, C. T.; Gonzalez-Fajardo, L.; Hargrove, D.; Song, D.; Deshmukh, P.; Mahajan, L.; Ndaya, D.; Lai, L.; Kasi, R. M.; Lu, X. Long Circulating Self-Assembled Nanoparticles from Cholesterol-Containing Brush-Like Block Copolymers for Improved Drug Delivery to Tumors. *Biomacromolecules* **2014**, *15*, 4363-4375.
- 43. Zou, J.; Yu, Y.; Li, Y. K.; Ji, W.; Chen, C. K.; Law, W. C.; Prasad, P. N.; Cheng, C. Well-Defined Diblock Brush Polymer-Drug Conjugates for Sustained Delivery of Paclitaxel. *Biomater. Sci.* **2015**, *3*, 1078-1084.
- 44. Johnson, J. A.; Lu, Y. Y.; Burts, A. O.; Xia, Y.; Durrell, A. C.; Tirrell, D. A.; Grubbs, R. H. Drug-Loaded, Bivalent-Bottle-Brush Polymers by Graft-Through ROMP. *Macromolecules* **2010**, *43*, 10326-10335.

- 45. Patel, P. R.; Kiser, R. C.; Lu, Y. Y.; Fong, E.; Ho, W. C.; Tirrell, D. A.; Grubbs, R. H. Synthesis and Cell Adhesive Properties of Linear and Cyclic RGD Functionalized Polynorbornene Thin Films. *Biomacromolecules* **2012**, *13*, 2546-2553.
- 46. Sankaran, N. B.; Rys, A. Z.; Nassif, R.; Nayak, M. K.; Metera, K.; Chen, B. Z.; Bazzi, H. S.; Sleiman, H. F. Ring-Opening Metathesis Polymers for Biodetection and Signal Amplification: Synthesis and Self-Assembly. *Macromolecules* **2010**, *43*, 5530-5537.
- 47. Vohidov, F.; Milling, L. E.; Chen, Q. X.; Zhang, W. X.; Bhagchandani, S.; Nguyen, H. V. T.; Irvine, D. J.; Johnson, J. A. ABC Triblock Bottlebrush Copolymer-Based Injectable Hydrogels: Design, Synthesis, and Application to Expanding the Therapeutic Index of Cancer Immunochemotherapy. *Chem. Sci.* **2020**, *11*, 5974-5986.
- 48. Rao, N. V.; Dinda, H.; Venu, P.; Das Sarma, J.; Shunmugam, R. Smart Nanocarrier from Norbornene Based Triblock Copolymers for the Sustained Release of Multi-Cancer Drugs. *RSC Adv.* **2014**, *4*, 45625-45634.
- 49. Newman, D. J.; Cragg, G. M. Natural Products as Sources of New Drugs over the Nearly Four Decades from 01/1981 to 09/2019. *J. Nat. Prod.* **2020**. *83*. 770-803.
- 50. Bezerra, D. P.; Pessoa, C.; de Moraes, M. O.; Saker-Neto, N.; Silveira, E. R.; Costa-Lotufo, L. V. Overview of the Therapeutic Potential of Piplartine (Piperlongumine). *Eur. J. Pharm. Sci.* **2013**, *48*, 453-463.
- 51. Tripathi, S. K.; Biswal, B. K. Piperlongumine, A Potent Anticancer Phytotherapeutic: Perspectives on Contemporary Status and Future Possibilities as an Anticancer Agent. *Pharmacol. Res.* **2020**, *156*, 104772.
- 52. Piska, K.; Gunia-Krzyzak, A.; Koczurkiewicz, P.; Wojcik-Pszczola, K.; Pekala, E. Piperlongumine (Piplartine) as a Lead Compound for Anticancer Agents Synthesis and Properties of Analogues: A Mini-Review. *Eur. J. Med. Chem.* **2018**, *156*, 13-20.
- 53. Bezerra, D. P.; Militao, G. C. G.; de Castro, F. O.; Pessoa, C.; de Moraes, M. O.; Silveira, E. R.; Lima, M. A. S.; Elmiro, F. J. M.; Costa-Lotufo, L. V. Piplartine Induces Inhibition of Leukemia Cell Proliferation Triggering Both Apoptosis and Necrosis Pathways. *Toxicol. in Vitro* **2007**, *21*, 1-8.
- 54. Barcelos, R. C.; Pastre, J. C.; Vendramini-Costa, D. B.; Caixeta, V.; Longato, G. B.; Monteiro, P. A.; de Carvalho, J. E.; Pilli, R. A. Design and Synthesis of *N*-Acylated Aza-Goniothalamin Derivatives and Evaluation of Their *In Vitro* and *In Vivo* Antitumor Activity. *ChemMedChem* **2014**, *9*, 2725-2743.
- 55. Dhillon, H.; Chikara, S.; Reindl, K. M. Piperlongumine Induces Pancreatic Cancer Cell Death by Enhancing Reactive Oxygen Species and DNA Damage. *Toxicol. Rep.* **2014**, *1*, 309-318.
- 56. Ginzburg, S.; Golovine, K. V.; Makhov, P. B.; Uzzo, R. G.; Kutikov, A.; Kolenko, V. M. Piperlongumine Inhibits NF-KappaB Activity and Attenuates Aggressive Growth Characteristics of Prostate Cancer Cells. *Prostate* **2014**, *74*, 177-186.
- 57. Zheng, J.; Son, D. J.; Gu, S. M.; Woo, J. R.; Ham, Y. W.; Lee, H. P.; Kim, W. J.; Jung, J. K.; Hong, J. T. Piperlongumine Inhibits Lung Tumor Growth Via Inhibition of Nuclear Factor Kappa B Signaling Pathway. *Sci. Rep.* **2016**, *6*, 26357.
- 58. Liao, Y.; Niu, X.; Chen, B.; Edwards, H.; Xu, L.; Xie, C.; Lin, H.; Polin, L.; Taub, J. W.; Ge, Y.; Qin, Z. Synthesis and Antileukemic Activities of Piperlongumine and HDAC Inhibitor Hybrids against Acute Myeloid Leukemia Cells. *J. Med. Chem.* **2016**, *59*, 7974-7990.
- 59. Bezerra, D. P.; Castro, F. O.; Alves, A. P.; Pessoa, C.; Moraes, M. O.; Silveira, E. R.; Lima, M. A.; Elmiro, F. J.; Costa-Lotufo, L. V. *In Vivo* Growth-Inhibition of Sarcoma 180 by Piplartine and Piperine, Two Alkaloid Amides from Piper. *Braz. J. Med. Biol. Res.* **2006**, *39*, 801-807.
- 60. Duan, C.; Zhang, B.; Deng, C.; Cao, Y.; Zhou, F.; Wu, L.; Chen, M.; Shen, S.; Xu, G.; Zhang, S.; Duan, G.; Yan, H.; Zou, X. Piperlongumine Induces Gastric Cancer Cell Apoptosis and G2/M Cell Cycle Arrest Both *In Vitro* and *In Vivo. Tumour Biol.* **2016**, *37*, 10793-10804.
- 61. Xiong, X. X.; Liu, J. M.; Qiu, X. Y.; Pan, F.; Yu, S. B.; Chen, X. Q. Piperlongumine Induces Apoptotic and Autophagic Death of the Primary Myeloid Leukemia Cells From Patients Via Activation of ROS-p38/JNK Pathways. *Acta Pharmacol. Sin.* **2015**, *36*, 362-374.
- 62. Adams, D. J.; Boskovic, Z. V.; Theriault, J. R.; Wang, A. J.; Stern, A. M.; Wagner, B. K.; Shamji, A. F.; Schreiber, S. L. Discovery of Small-

- Molecule Enhancers of Reactive Oxygen Species That Are Nontoxic or Cause Genotype-Selective Cell Death. ACS Chem. Biol. 2013, 8, 923-929.
- 63. Adams, D. J.; Dai, M.; Pellegrino, G.; Wagner, B. K.; Stern, A. M.; Shamji, A. F.; Schreiber, S. L. Synthesis, Cellular Evaluation, and Mechanism of Action of Piperlongumine Analogs. *Proc. Natl Acad. Sci. U. S. A.* **2012**, *109*, 15115-15120.
- 64. Aodah, A.; Pavlik, A.; Karlage, K.; Myrdal, P. B. Preformulation Studies on Piperlongumine. *PloS One* **2016**, *11*, e0151707.
- 65. Choi, T. L.; Grubbs, R. H. Controlled Living Ring-Opening-Metathesis Polymerization by a Fast-Initiating Ruthenium Catalyst. *Angew. Chem. Int. Ed.* **2003**, *42*, 1743-1746.
- 66. Pollino, J. M.; Stubbs, L. P.; Weck, M. Living ROMP of Exo-Norbornene Esters Possessing (PdSCS)-S-II Pincer Complexes or Diaminopyridines. *Macromolecules* **2003**, *36*, 2230-2234.
- 67. Spring, A. M.; Qiu, F.; Hong, J. X.; Bannaron, A.; Yokoyama, S. Electro-Optic Properties of a Side Chain Poly(norbornene-dicarboximide) System With an Appended Phenyl Vinylene Thiophene Chromophore. *Polymer* **2017**, *119*, 13-27.
- 68. Moatsou, D.; Hansell, C. F.; O'Reilly, R. K. Precision Polymers: A Kinetic Approach for Functional Poly(norbornenes). *Chem. Sci.* **2014**, *5*, 2246-2250.
- 69. Bates, C. M.; Chang, A. B.; Momcilovic, N.; Jones, S. C.; Grubbs, R. H. ABA Triblock Brush Polymers: Synthesis, Self-Assembly, Conductivity, and Rheological Properties. *Macromolecules* **2015**, *48*, 4967-4973.
- 70. Slugovc, C. The Ring Opening Metathesis Polymerisation Toolbox. *Macromol. Rapid Commun.* **2004**, *25*, 1283-1297.
- 71. Zhang, C.; Liu, T.; Su, Y.; Luo, S.; Zhu, Y.; Tan, X.; Fan, S.; Zhang, L.; Zhou, Y.; Cheng, T.; Shi, C. A Near-Infrared Fluorescent Heptamethine Indocyanine Dye With Preferential Tumor Accumulation for *In Vivo* Imaging. *Biomaterials* **2010**, *31*, 6612-6617.
- 72. Zhang, E.; Luo, S.; Tan, X.; Shi, C. Mechanistic Study of IR-780 Dye as a Potential Tumor Targeting and Drug Delivery Agent. *Biomaterials* **2014**, *35*, 771-778.
- 73. Braga, C. B.; Perli, G.; Becher, T. B.; Omelas, C. Biodegradable and pH-Responsive Acetalated Dextran (Ac-Dex) Nanoparticles for NIR Imaging and Controlled Delivery of a Platinum-Based Prodrug into Cancer Cells. *Mol. Pharmaceutics* **2019**, *16*, 2083-2094.
- 74. Wang, Y.; Weng, J.; Lin, J.; Ye, D.; Zhang, Y. NIR Scaffold Bearing Three Handles for Biocompatible Sequential Click Installation of Multiple Functional Arms. *J. Am. Chem. Soc.* **2020**, *142*, 2787-2794.
- 75. Ornelas, C.; Pennell, R.; Liebes, L. F.; Weck, M. Construction of a Well-Defined Multifunctional Dendrimer for Theranostics. *Org. Lett.* **2011**, *13*, 976-979.
- 76. Choi, P. J.; Park, T. I. H.; Cooper, E.; Dragunow, M.; Denny, W. A.; Jose, J. Heptamethine Cyanine Dye Mediated Drug Delivery: Hype or Hope. *Bioconjugate Chem.* **2020**, *31*, 1724-1739.
- 77. Weinstain, R.; Slanina, T.; Kand, D.; Klan, P. Visible-to-NIR-Light Activated Release: From Small Molecules to Nanomaterials. *Chem. Rev.* **2020**, *120*, 13135-13272.
- 78. Strekowski, L.; Lipowska, M.; Patonay, G. Substitution-Reactions of a Nucleofugal Group in Heptamethine Cyanine Dyes Synthesis of an Isothiocyanato Derivative for Labeling of Proteins with a near-Infrared Chromophore. *J. Org. Chem.* **1992**, *57*, 4578-4580.
- 79. Grigolo, T. G.; Braga, C. B.; Ornelas, C.; Russowsky, D.; Ferreira-Silva, G. A.; Ionta, M.; Pilli, R. A. Synthesis and *In Vitro* Antineoplastic Evaluation of Goniothalamin-Monastrol and Piplartine-Monastrol Hybrids. Unpublished Results (Manuscript under revision), 2021. Hybrids of 4-Hydroxy Derivatives of Goniothalamin and Piplartine Bearing a Diester or a 1,2,3-Triazole Linker as Antiproliferative Agents. *Bioorg. Chem.* **2021**, DOI: 10.1016/j.bioorg.2021.105292.
- 80. Fliervoet, L. A. L.; Najafi, M.; Hembury, M.; Vermonden, T. Heterofunctional Poly(ethylene glycol) (PEG) Macroinitiator Enabling Controlled Synthesis of ABC Triblock Copolymers. *Macromolecules* **2017**, *50*, 8390-8397. Agard, N. J.; Prescher, J. A.; Bertozzi, C. R. A Strain-Promoted

- [3 + 2] Azide-Alkyne Cycloaddition for Covalent Modification of Biomolecules in Living Systems. *J. Am. Chem. Soc.* **2004**, *126*, 15046-15047.
- 81. Agard, N.J.; Prescher, J. A.; Bertozzi, C. R. A Strain-Promoted [3 + 2] Azide-Alkyne Cycloaddition for Covalent Modification of Biomolecules in Living Systems. *J. Am. Chem. Soc.* **2004**, *126*, 15046-15047. Sletten, E. M.; Bertozzi, C. R. Bioorthogonal Chemistry: Fishing for Selectivity in a Sea of Functionality. *Angew. Chem. Int. Ed.* **2009**, *48*, 6974-6998
- 82. Sletten, E. M.; Bertozzi, C. R. Bioorthogonal Chemistry: Fishing for Selectivity in a Sea of Functionality. *Angew. Chem. Int. Ed.* **2009**, *48*, 6974-6998. Kennedy, D. C.; McKay, C. S.; Legault, M. C. B.; Danielson, D. C.; Blake, J. A.; Pegoraro, A. F.; Stolow, A.; Mester, Z.; Pezacki, J. P. Cellular Consequences of Copper Complexes Used To Catalyze Bioorthogonal Click Reactions. *J. Am. Chem. Soc.* **2011**, *133*, 17993-18001.
- 83. Kennedy, D. C.; McKay, C. S.; Legault, M. C. B.; Danielson, D. C.; Blake, J. A.; Pegoraro, A. F.; Stolow, A.; Mester, Z.; Pezacki, J. P. Cellular Consequences of Copper Complexes Used To Catalyze Bioorthogonal Click Reactions. *J. Am. Chem. Soc.* **2011**, *133*, 17993-18001. Abel, G. R.; Calabrese, Z. A.; Ayco, J.; Hein, J. E.; Ye, T. Measuring and Suppressing the Oxidative Damage to DNA During Cu(I)-Catalyzed Azide-Alkyne Cycloaddition. *Bioconjugate Chem.* **2016**, *27*, 698-704.
- 84. Abel, G. R.; Calabrese, Z. A.; Ayco, J.; Hein, J. E.; Ye, T. Measuring and Suppressing the Oxidative Damage to DNA During Cu(I)-Catalyzed Azide-Alkyne Cycloaddition. *Bioconjugate Chem.* **2016**, *27*, 698-704. Dommerholt, J.; Schmidt, S.; Temming, R.; Hendriks, L. J.; Rutjes, F. P.; van Hest, J. C.; Lefeber, D. J.; Friedl, P.; van Delft, F. L. Readily Accessible Bicyclononynes for Bioorthogonal Labeling and Three-Dimensional Imaging of Living Cells. *Angew. Chem. Int. Ed.* **2010**, *49*, 9422-9425.
- 85. Dommerholt, J.; Schmidt, S.; Temming, R.; Hendriks, L. J.; Rutjes, F. P.; van Hest, J. C.; Lefeber, D. J.; Friedl, P.; van Delft, F. L. Readily Accessible Bicyclononynes for Bioorthogonal Labeling and Three-Dimensional Imaging of Living Cells. *Angew. Chem. Int. Ed.* **2010**, *49*, 9422-9425. Fenyves, R.; Schmutz, M.; Horner, I. J.; Bright, F. V.; Rzayev, J. *J. Am. Chem. Soc.* **2014**, *136*, 7762–7770.
- 86. Discher, D. E.; Eisenberg, A. Polymer Vesicles. *Science* **2002**, *297*, 967-73. Yao, Q.; Gutierrez, D. C.; Hoang, N. H.; Kim, D.; Wang, R.; Hobbs, C.; Zhu, L. Efficient Codelivery of Paclitaxel and Curcumin by Novel Bottlebrush Copolymer-Based Micelles. *Mol. Pharmaceutics* **2017**, *14*, 2378-2389.
- 87. Yao, Q.; Gutierrez, D. C.; Hoang, N. H.; Kim, D.; Wang, R.; Hobbs, C.; Zhu, L. Efficient Codelivery of Paclitaxel and Curcumin by Novel Bottlebrush Copolymer-Based Micelles. *Mol. Pharmaceutics* **2017**, *14*, 2378-2389. Takano, S.; Islam, W.; Nakazawa, K.; Maeda, H.; Sakurai, K.; Fujii, S. Phosphorylcholine-Grafted Molecular Bottlebrush-Doxorubicin Conjugates: High Structural Stability, Long Circulation in Blood, and Efficient Anticancer Activity. *Biomacromolecules* **2021**, *22*, 1186-1196.
- 88. Takano, S.; Islam, W.; Nakazawa, K.; Maeda, H.; Sakurai, K.; Fujii, S. Phosphorylcholine-Grafted Molecular Bottlebrush-Doxorubicin Conjugates: High Structural Stability, Long Circulation in Blood, and Efficient Anticancer Activity. *Biomacromolecules* **2021**, *22*, 1186-1196. Peng, X. J.; Song, F. L.; Lu, E.; Wang, Y. N.; Zhou, W.; Fan, J. L.; Gao, Y. L. Heptamethine Cyanine Dyes With a Large Stokes Shift and Strong Fluorescence: A Paradigm for Excited-State Intramolecular Charge Transfer. *J. Am. Chem. Soc.* **2005**, *127*, 4170-4171.
- 89. Peng, X. J.; Song, F. L.; Lu, E.; Wang, Y. N.; Zhou, W.; Fan, J. L.; Gao, Y. L. Heptamethine Cyanine Dyes With a Large Stokes Shift and Strong Fluorescence: A Paradigm for Excited-State Intramolecular Charge Transfer. *J. Am. Chem. Soc.* **2005**, *127*, 4170-4171. Sissa, C.; Painelli, A.; Terenziani, F.; Trotta, M.; Ragni, R. About the Origin of the Large Stokes Shift in Aminoalkyl Substituted Heptamethine Cyanine Dyes. *Phys. Chem. Chem. Phys.* **2019**, *22*, 129-135.
- 90. Sissa, C.; Painelli, A.; Terenziani, F.; Trotta, M.; Ragni, R. About the Origin of the Large Stokes Shift in Aminoalkyl Substituted Heptamethine Cyanine Dyes. *Phys. Chem. Chem. Phys.* **2019**, *22*, 129-135.

# Table of Contents graphic

